

# Coca-Splat: Collaborative Optimization for Camera Parameters and 3D Gaussians

Jiamin Wu<sup>1,2\*</sup>, Hongyang Li<sup>2</sup>, Xiaoke Jiang<sup>2†</sup>, Yuan YAO<sup>1</sup>, Lei Zhang<sup>2</sup>

<sup>1</sup>Hong Kong University of Science and Technology

<sup>2</sup>International Digital Economy Academy (IDEA)

## Abstract

In this work, we introduce **Coca-Splat**, a novel approach to addressing the challenges of sparse view pose-free scene reconstruction and novel view synthesis (NVS) by jointly optimizing camera parameters with 3D Gaussians. Inspired by deformable DETection TRansformer, we design separate queries for 3D Gaussians and camera parameters and update them layer by layer through deformable Transformer layers, enabling joint optimization in a single network. This design demonstrates better performance because to accurately render views that closely approximate ground-truth images relies on precise estimation of both 3D Gaussians and camera parameters. In such a design, the centers of 3D Gaussians are projected onto each view by camera parameters to get projected points, which are regarded as 2D reference points in deformable cross-attention. With camera-aware multi-view deformable cross-attention (**CaMDFA**), 3D Gaussians and camera parameters are intrinsically connected by sharing the 2D reference points. Additionally, 2D reference point determined rays (**RayRef**) defined from camera centers to the reference points assist in modeling relationship between 3D Gaussians and camera parameters through RQ-decomposition on an overdetermined system of equations derived from the rays, enhancing the relationship between 3D Gaussians and camera parameters. Extensive evaluation shows that our approach outperforms previous methods, both pose-required and pose-free, on RealEstate10K and ACID within the same pose-free setting.

## 1 Introduction

Sparse view scene reconstruction, novel view synthesis (NVS), and input view pose estimation represent crucial challenges in computer vision with wide-ranging applications in robotics, augmented reality (AR), virtual reality (VR), games, and films. Recent advancements in differentiable rendering techniques such as Neural Radiance Fields (NeRF) (Mildenhall et al., 2020; Zhang et al., 2020) and 3D Gaussian Splatting (3DGS) (Kerbl et al., 2023; Chen and Wang, 2024) have enabled rapid progress in scene reconstruction and NVS using deep learning methods, relying solely on 2D supervision due to difficulty in obtaining 3D assets for supervision. Recent methods like pixelSplat (Charatan et al., 2024) and MVSplat (Chen, Yuedong and Xu, Haofei and Zheng, Chuanxia and Zhuang, Bohan and Pollefeys, Marc and Geiger, Andreas and Cham, Tat-Jen and Cai, Jianfei, 2024) take advantage of fast rendering speed of 3DGS to achieve precise scene reconstruction and NVS within approximately one second. However, these methods require ground truth camera poses for input views, posing challenges in real-world scenarios. While these poses can be derived from dense videos using structure-from-motion (SfM) methods (Schonberger and Frahm, 2016; Hartley and Zisserman, 2004; Snavely et al., 2006), inaccurate pose estimation may impact performance and increase inference time.

\*This work is done during an internship in the International Digital Economy Academy (IDEA).

†Corresponding author

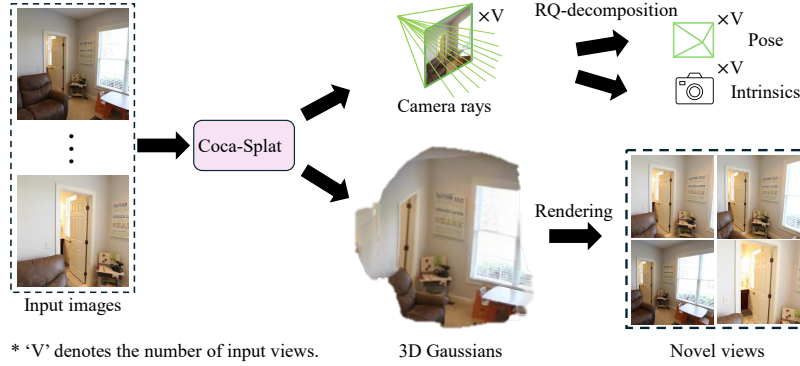


**Figure 1: Coca-Splat.** Given sparse unposed images, our method reconstructs 3D Gaussians and camera rays using a feed-forward network. Subsequently, camera parameters are derived from camera rays, and novel views are rendered from 3D Gaussians.

Recent methods focusing on pose-free scene reconstruction are increasingly suitable for real-world applications, falling into two main categories. The first category involves pose-free scene reconstruction and NVS methods like Ye et al. (2025); Xu et al. (2024a); Wang et al. (2024); Leroy et al. (2024); Smart et al. (2024); Wang et al. (2023b); Liu et al. (2024a) which do not explicitly incorporate pose information in the network architecture. Instead, they generate scenes based on image feature matching and comparison while utilizing post-processing techniques, such as Perspective-n-Point (PnP) algorithm (Hartley and Zisserman, 2004), for calculating input poses. The second category includes methods like Jiang et al. (2024); Bian et al. (2023); Kang et al. (2024); Chen and Lee (2023); Smith et al. (2023); Hong et al. (2024b) which employ separate pose estimators for pose estimation and 3D estimators for scene reconstruction but obtain pose and scene information in a unified pipeline. Some of these methods combine predicted pose and 3D information to optimize re-projection error or rendered RGB error for enhanced results.

However, the separation of camera parameter estimation and scene reconstruction in such approaches often leads to suboptimal results since only precise reconstructions of both 3D scenes and camera parameters can result in novel views that closely approximate ground truth. This separation not only lengthens the pipeline but also introduces a compounding effect: errors in camera parameters estimation can deteriorate scene reconstruction, leading to additional inaccuracies in camera parameters estimation (Ye et al., 2025).

In this study, we introduce **Coca-Splat** to jointly estimate camera parameters of input views and synthesize novel views for scenes by directly connecting camera parameters with 3D Gaussians within a single network as shown in Fig. 1. Inspired by GeoLRM (Zhang et al., 2024a), LeanGaussian (Wu et al., 2025) and UNIG (Wu et al., 2024), which leverage the Deformable DETection TRansformer (Deformable DETR) (Zhu et al., 2021) framework in 3D, we introduce separate queries for 3D Gaussians and camera parameters (3D queries and camera queries in short). The 3D queries are utilized to generate 3D Gaussians by multi-layer perceptron (MLP), while the camera queries are employed to regress camera extrinsics and intrinsics using our introduced **RefRay** (2D reference point determined rays) representation on the camera queries. 3D Gaussians (center of them) are then projected onto each view using camera parameters, and the projected points are regarded as 2D reference points in deformable cross-attention. Subsequently, both 3D and camera queries are updated by deformable cross-attention with image features surrounding these 2D reference points. The above process is called **CaMDFA** (camera-aware multi-view deformable cross-attention), which efficiently establishes a connection between 3D Gaussians and camera parameters through 2D reference points, updating them effectively.

Although the model effectively optimizes 3D Gaussians and camera parameters jointly, a **challenge** arises when regressing camera parameters directly from numerous parameters (resulting from multiplication of the number of reference points by hidden dimension). This approach may not be optimal for neural learning, which typically benefits from over-parameterized distributed representations (Zhang et al., 2024c). Inspired by Ray-Diffusion (Zhang et al., 2024c), which represents camera parameters as rays from camera center to each pixel on a image, we design **RefRay**, modeling camera parameters as

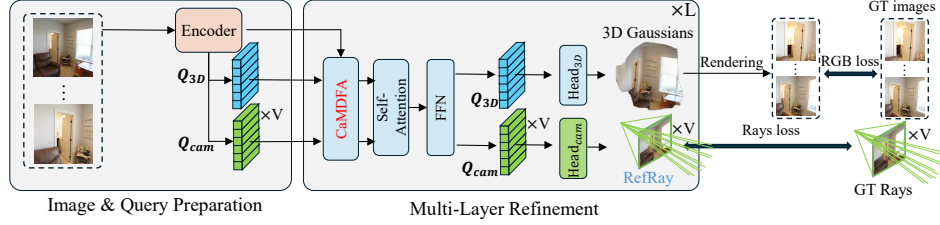


**Figure 2:** Overall Framework: Our model employs an encoder-decoder architecture to simultaneously reconstruct 3D Gaussians and camera parameters. The Vision Transformer (ViT) encoder processes all input images, with the resulting image features serving as keys and values in **CaMDFA** block (Section 3.3) within the decoder layer. In our approach, define queries for 3D Gaussians and camera queries separately, incorporating them into the deformable decoder layer alongside the image features. Following  $L$  decoder layers, the model produces queries for 3D Gaussians and cameras, which are used to go through a fully connected network (FFN) operation to regress the 3D Gaussians and **RefRay** (in Plücker coordinates (Plücker, 1828) denoting the direction and moment Section 3.4) that points from camera center to reference points. Subsequently, the predicted 3D Gaussians undergo rendering via Gaussian Splatting (Kerbl et al., 2023) to generate the novel views while the rays are utilized to solve the camera parameters in Section 3.4.

rays from camera center to the 2D reference points on each input view and design an overdetermined equation system using equations of the rays to solve camera parameters. With the aforementioned design, our model solves both camera extrinsics and intrinsics through RQ-decomposition, enabling scene reconstruction without the need for any input view camera parameters.

With the aforementioned design, our model effectively establishes a direct connection between 3D Gaussians and camera parameters through a **shared set** of 2D reference points, enabling joint optimization. The collaboration of 3D Gaussians and camera parameters plays an important role in the 3D Gaussian reconstruction and NVS outcomes.

In summary, our contributions are as follows:

- We propose a novel approach to modeling 3D Gaussians and camera poses of input views jointly without any pre-processing or post-processing steps, making scene reconstruction without any input view camera parameters.
- We establish a direct connection between 3D Gaussians and camera parameters through 2D reference points and using **CaMDFA** and **RefRay** to optimize both 3D Gaussians and camera parameters possible.
- Our method outperforms previous methods, both pose-required and pose-free, on RealEstate10K (RE10K) (Zhou et al., 2018) and ACID (Liu et al., 2021) within the same pose-free setting.

## 2 Related Work

**Pose required scene reconstruction NVS** The field of deep learning-based NVS has seen rapid advancement recently, driven by differentiable rendering techniques like NeRF (Mildenhall et al., 2020) and 3DGS (Kerbl et al., 2023). Subsequent methods, such as Yariv et al. (2021); Barron et al. (2021); Garbin et al. (2021); Rakotosaona et al. (2023); Yu et al. (2021); Müller et al. (2022); Li et al. (2023); Xu et al. (2024b); Zou et al. (2024); Zhang et al. (2024d,a); Tang et al. (2024); Long et al. (2024); Chen, Yuedong and Xu, Haoifei and Zheng, Chuanxia and Zhuang, Bohan and Pollefeys, Marc and Geiger, Andreas and Cham, Tat-Jen and Cai, Jianfei (2024); Charatan et al. (2024); Wu et al. (2025, 2024); Xu et al. (2024c); Zhu et al. (2022, 2024); Matsuki et al. (2024), have introduced novel deep learning models for this task. While some approaches take a single-view image as input but lack finer details, others accept multi-view images but necessitate ground truth camera poses, limiting real-world applicability. Methods like LGM and InstantMesh (Tang et al., 2024; Xu et al., 2024b) leverage single-view inputs and utilize diffusion models (Rombach et al., 2022; Wang and Shi, 2023; Shi et al., 2024) to generate fixed views (e.g., front, right, back, left) before applying their models, exploiting the ease of obtaining poses for these predetermined views. However, the generated views

may introduce uncertainties and distortions compared to real-world scenarios due to the reliance on diffusion models. Some methods leverage off-the-shelf SfM techniques (Schonberger and Frahm, 2016; Hartley and Zisserman, 2004; Snavely et al., 2006) to estimate input view poses. Nevertheless, this approach demands a denser array of views to achieve comparatively accurate estimations, and also increase the complexity of the process.

**Pose-free scene reconstruction and NVS** Liu et al. (2024b) do not need pose input for scene NVS but instead require per-scene optimization. Pose-free methods without per-scene optimization can generally be categorized into two groups. The first group comprises methods (Wang et al., 2021; Chen and Lee, 2023; Chng et al., 2022; Xu et al., 2024a; Hong et al., 2024b; Smith et al., 2023; Bian et al., 2023; Yu et al., 2024; Hong et al., 2024a; Sajjadi et al., 2022) that optimize pose and scene simultaneously. However, these methods typically employ separate networks to estimate them, often lacking direct connections between them or relying on initializations from other pose and scene prediction models. This can lead to complex pipelines and a lack of explicit connections between pose and scene. The second category includes methods (Wang et al., 2024; Leroy et al., 2024; Ye et al., 2025; Smart et al., 2024; Zhang et al., 2024b) which initially reconstruct the scene in a canonical space without explicit pose input, rely on point or feature matching for scene reconstruction. Subsequently, the PnP algorithm is used to compute camera poses by matching points reconstructed from different input views, requiring sufficient overlap between input views and do pose-processing for pose estimation. Techniques for object reconstruction (Wang et al., 2023b; Jiang et al., 2024, 2023) often involve lifting each pixel to a 3D Gaussian or relying on voxel representations, limiting input resolution and efficiency. In contrast, our model optimizes scene and pose jointly without additional pipelines. The comparison between our method and representative previous methods is in Table 1 with more methods comparison in Appendix A.1.1 Table 7.

**Model-free pose estimation** Methods like Zhang et al. (2022); Lin et al. (2024); Zhang et al. (2024c); Wen et al. (2024); Wang et al. (2023a); Wen et al. (2023) directly regress poses from input images without 3D models. Many of these techniques leverage tools such as cross-attention and cost-volume to compare variations and similarities between different views and utilize the matching outcomes to estimate camera poses. However, lacking the assistance of 3D models, these methods are generally less effective compared to those incorporating 3D models. Some methods (Wang et al., 2019; Krishnan et al., 2024) utilize Normalized Object Coordinate Space (NOCS) for pose estimation. However, the reliance on well-aligned datasets that defines the positive direction for each object restricts its applicability.

Table 1: Comparison with representative methods. ‘Pose-Free’ means that the model is pose-free, ‘Jointly Opt’ means that the model optimize camera and 3D jointly, ‘Cano. Space’ means that the model define 3D points in the canonical space for all views, ‘Intri.-Free’ means that the model does not require intrinsic input, ‘3D GS’ means the model use 3D Gaussians as 3D representation.

Method	Pose-Free	Jointly Opt.	Cano. Space	Intri.-Free	3D GS
MVSplat	✗	✗	✗	✗	✓
CoPoNeRF	✓	✓	✓	✗	✗
SelfSplat	✓	✗	✗	✗	✓
NoPoSplat	✓	✗	✓	✗	✓
Ours	✓	✓	✓	✓	✓

### 3 Methods

The details of our proposed method are given in this section. First, the preliminaries for 3D GS are briefly described in Section 3.1. Then, an overview of Coca-Splat is in Section 3.2. After that, Camera-aware Multi-view DeFormable cross-Attention (CaMDFA) module, the core contribution of Coca-Splat is described in Section 3.3 in detail. Moreover, the definition of 2D reference point determined rays RefRay, which is proposed to represent the camera parameters in Coca-Splat, is introduced in Section 3.4. Finally, the training objective is introduced in Section 3.5.

### 3.1 Preliminaries of 3D GS

3D GS (Kerbl et al., 2023) is a rendering method that utilize 3D Gaussians to represent 3D objects or scenes. In this context, a scene which consists of  $N$  3D Gaussians can be represented as a set of parameters  $\{\mathbf{SH}, \boldsymbol{\mu}, \boldsymbol{\sigma}, \mathbf{R}, \mathbf{S}\}$ . The color of a 3D Gaussian ellipsoid is represented by spherical harmonics ( $\mathbf{SH}$ )  $\in \mathbb{R}^{N \times k}$  (Dai et al., 2013; Kerbl et al., 2023), with degree of freedom  $k$ , while the geometry is described by position  $\boldsymbol{\mu} \in \mathbb{R}^{N \times 3}$ , shape (including rotation  $\mathbf{R} \in \mathbb{R}^{N \times 4}$  in quaternion and scales  $\mathbf{S} \in \mathbb{R}^{N \times 3}$ ), and opacity  $\boldsymbol{\sigma} \in \mathbb{R}^N$  (Zwicker et al., 2001; Kerbl et al., 2023). Therefore, the objective of 3D Gaussian reconstruction is to estimate the aforementioned parameters for 3D Gaussians.

### 3.2 Overview of Coca-Splat

**Image feature preparation.** Following Wang et al. (2024); Leroy et al. (2024); Ye et al. (2025), we utilize the Vision Transformer (ViT) (Dosovitskiy et al., 2021) to extract multi-view image features from input images. The input images are first patchified and flattened to sequences of image tokens, which are then sent into ViT layers to derive the multi-view image features  $\mathbf{F}$ . To expedite convergence, we initialize our ViT encoder based on NoPoSplatYe et al. (2025).

**Query preparation for 3D Gaussians and camera parameters.** As mentioned in Section 1, our model define separate queries for 3D Gaussians and camera parameters as 3D queries  $\mathbf{Q}_{3D} \in \mathbb{R}^{N \times D}$  and camera queries  $\mathbf{Q}_{cam} \in \mathbb{R}^{V \times N \times D}$  respectively, where  $N$  denotes the number of queries, which is also the number of 3D Gaussians,  $V$  is the number of input views. Note that both queries share the same locations as the centers of 3D Gaussians and therefore share the same set of 2D reference points after projection. The 3D Gaussian queries' corresponding 3D Gaussian parameters  $\mathbf{G} \in \mathbb{R}^{N \times K}$  are obtained by conducting an MLP on  $\mathbf{Q}_{3D}$ , where  $K$  denotes the dimension of 3D Gaussian parameters. The camera queries' corresponding RefRay  $\mathcal{R} \in \mathbb{R}^{V \times N \times 6}$ , which is the intermediate representation of camera parameters (see Section 3.4), are obtained by conducting MLP on  $\mathbf{Q}_{cam}$ . The 3D queries are initialized from the flattening image features from ViT (see Appendix A.4 for more details). The camera queries are randomly initialized as learnable vectors.

**Multi-layer refinement.** As shown in Fig. 2, within the multi-layer refinement, our method focuses on the optimization of 3D Gaussians  $\mathbf{G}$  and camera RefRay  $\mathcal{R}$  in each layer. As shown in Fig. 2, 3D queries and camera queries first pass through a camera-aware multi-view deformable cross-attention (CaMDFA) block, where the multi-view image features from the ViT encoder contribute as keys and values, as detailed in Section 3.3. Subsequently, the updated 3D queries and camera queries conduct self-attention individually. In particular, to mitigate memory costs, we implement a spatially efficient self-attention strategy inspired by UniG(Wu et al., 2024) (for more details, please refer to Appendix A.3. After that, the queries are updated by feed-forward networks (FFNs). The progress for updating queries in the  $l$ -th layer can be formulated as

$$\begin{aligned} \mathbf{Q}_{3D}^l, \mathbf{Q}_{cam}^l &= \text{CaMDFA}(\mathbf{Q}_{3D}^{l-1}, \mathbf{Q}_{cam}^{l-1}, \mathbf{P}^l, \mathbf{F}), \\ \mathbf{Q}_{3D}^l &= \text{FFN}(\text{SA}(\mathbf{Q}_{3D}^l)), \quad \mathbf{Q}_{cam}^l = \text{FFN}(\text{SA}(\mathbf{Q}_{cam}^l)) \end{aligned} \quad (1)$$

where SA representing the self-attention layer and  $\mathbf{P}^l$  indicates 2D reference points in the  $l$ -th layer (refer to details in Section 3.3). Finally, the updated 3D queries are utilized to refine the 3D Gaussians by Eq. (2),

$$\mathbf{G}^l = \Delta \mathbf{G}^l + \mathbf{G}^{l-1}, \Delta \mathbf{G}^l = \text{Head}_{3D}(\mathbf{Q}_{3D}^l) \quad (2)$$

where  $\mathbf{G}^l$  is the parameters of 3D Gaussians in current layer<sup>3</sup>,  $\text{Head}_{3D}$  is an MLP. Meanwhile, camera queries are utilized to update camera parameters, with the intermediate representation RefRay (see Section 3.4) as shown in Eq. (3),

$$\mathcal{R}^l = \Delta \mathcal{R}^l + \mathcal{R}^{l-1}, \Delta \mathcal{R}^l = \text{Head}_{cam}(\mathbf{Q}_{cam}^l) \quad (3)$$

where  $\mathcal{R}^l$  denotes RefRay in current layer<sup>4</sup>, and  $\text{Head}_{cam}$  is an MLP. After that the camera parameters  $\mathbf{K}^l$  and  $\boldsymbol{\pi}^l$  are updated by the ray representation RefRay  $\mathcal{R}^l$  (see Section 3.4 and Appendix A.2), and then they are passed into the next layer for 2D reference projection as in Eq. (4).

<sup>3</sup>In the first layer,  $\mathbf{G}^{l-1}$  is initialized by conducting an MLP on the initialized 3D queries.

<sup>4</sup>In the first layer,  $\mathcal{R}^{l-1}$  is initialized from initial camera parameters, which are defined as identity matrices.

### 3.3 CaMDFA

**2D reference points in CaMDFA.** As mentioned in Section 3.2, 2D reference points in CaMDFA are defined as the projected points of 3D Gaussians. Specifically, 2D reference points on the  $i$ -th view are generated by projecting the center of 3D Gaussians onto the  $i$ -th view, using the pinhole camera model (Forsyth and Ponce, 2003; Hartley and Zisserman, 2003), as shown in Fig. 3 and Eq. (4),

$$\mathbf{P}_i = \mathbf{K}_i \boldsymbol{\pi}_i \boldsymbol{\mu} \quad (4)$$

where  $\mathbf{P}_i$  represents the 2D reference points on the  $i$ -th view,  $\boldsymbol{\pi}_i$  is the camera extrinsics, and  $\mathbf{K}_i$  is camera intrinsics of the  $i$ -th view.

**Query updating for 3D Gaussian in CaMDFA.** The locations of the 3D Gaussian queries are defined in canonical space<sup>5</sup> unitarily rather than individually for each view. Sharing the queries across multi-views directly is impractical. Inspired by Wu et al. (2024), we consider incorporating camera information for each view. Specifically, we employ camera modulation with adaptive layer norm (adaLN) (Hong et al., 2024c; Karras et al., 2019, 2020; Viazovetskyi et al., 2020) to derive 3D queries for the  $i$ -th view as shown in Eq. (5),

$$\begin{aligned} \mathbf{Q}_{3D_i} &= \text{LayerNorm}(\mathbf{Q}_{3D}) * (1 + \text{scale}) + \text{shift}, \\ \text{shift, scale} &= \text{MLP}(\mathbf{Q}_{cam_i}) \end{aligned} \quad (5)$$

The 3D queries are refined by conducting deformable cross-attention (DFA) on it with image features sampled surrounding the 2D reference points  $\mathbf{P}_i$  (see Eq. (4)) in the  $i$ -th view as keys and values as shown in Eq. (6),

$$\mathbf{Q}_{3D_i} = \text{DFA}(\mathbf{Q}_{3D_i}, \mathbf{P}_i, \mathbf{F}_i) \quad (6)$$

where  $\mathbf{F}_i$  is the image feature for the  $i$ -th view, DFA is the deformable cross-attention (see details in Appendix A.5). After refining the 3D queries for each view, it is essential to merge them to derive the unitary 3D queries. In alignment with Wu et al. (2024), we utilize a weighted sum by Eq. (7).

$$\mathbf{Q}_{3D} = \sum_i w_i \mathbf{Q}_{3D_i}, w_i = \text{sigmoid}(\text{MLP}(\mathbf{Q}_{3D_i})). \quad (7)$$

**Query updating for camera parameters in CaMDFA.** Instead of defining in canonical space like the 3D Gaussian queries, the camera queries are individually defined for each view. Meanwhile, the pose of each camera is specified relative to the reference view (defined as the 1-th view in our scenario without loss of generality). Therefore, to update camera queries for the  $i$ -th view, we only consider the 1-th and the  $i$ -th view as shown in Eq. (8).

$$\begin{aligned} \mathbf{Q}_{cam_i} &\Leftarrow \text{DFA}(\mathbf{Q}_{cam_i}, \mathbf{P}_{cam_i}, \mathbf{F}_i) \\ \mathbf{Q}_{cam_1} &\Leftarrow \text{DFA}(\mathbf{Q}_{cam_1}, \mathbf{P}_{cam_1}, \mathbf{F}_i). \end{aligned} \quad (8)$$

After refining  $\mathbf{Q}_{cam_1}$  and  $\mathbf{Q}_{cam_i}$ , our model performs an extra dense cross-attention to fuse them as shown in Eq. (9),

$$\begin{aligned} \mathbf{Q}_{cam_i} &\Leftarrow \mathbf{A}_i \cdot \mathbf{W}^V \mathbf{Q}_{cam_1}, \\ \mathbf{A}_i &= \text{softmax} \left( \frac{\mathbf{W}^Q \mathbf{Q}_{cam_i} \cdot (\mathbf{W}^K \mathbf{Q}_{cam_1})^T}{\sqrt{d_k}} \right) \end{aligned} \quad (9)$$

where  $\mathbf{W}^Q, \mathbf{W}^k, \mathbf{W}^V$  denotes transformation matrices, and  $d_k$  is the dimension of keys.

**Insights in CaMDFA.** The objective of CaMDFA is to link 3D Gaussians and camera parameters explicitly by sharing the same set of the projected 2D reference points. With the constraint in Eq. (4), 3D Gaussians (with the centers  $\boldsymbol{\mu}$ ) and camera parameters ( $\mathbf{K}, \boldsymbol{\pi}$ ) are optimized simultaneously. This joint optimization aids in obtaining more meaningful 2D reference points and subsequently extracting more relevant image features from multi-view images.

<sup>5</sup>The canonical space is defined as one input view’s local camera coordinates (Ye et al., 2025), and the selected input view is called reference view.

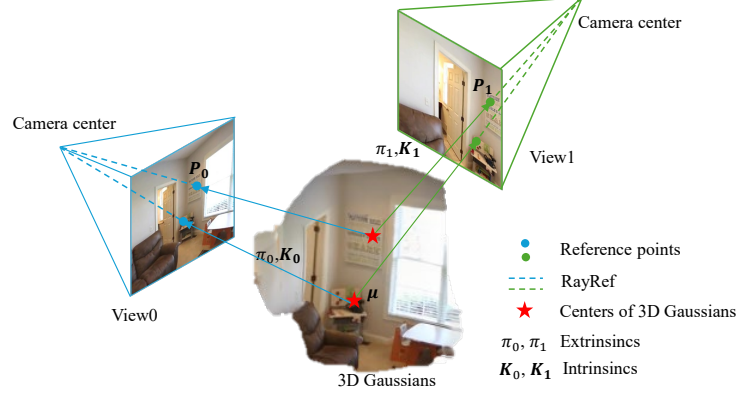


**Figure 3:** Our model projects the center of 3D Gaussians onto each input view by the camera parameters to get the reference points. The reference points are utilized to generate RefRay described in Section 3.4, which are the rays from the camera center to reference points. The 3D Gaussians and camera parameters are then explicitly linked by the reference points.

### 3.4 RefRay and Plücker-Camera sparse mapping

Typically, camera for the  $i$ -th view is parameterized by extrinsics  $\pi_i$  (consisting of rotations  $\pi_{iR} \in SO(3)$  and translations  $\pi_{iT} \in \mathbb{R}^3$ ) and intrinsics  $\mathbf{K}_i \in \mathbb{R}^{3 \times 3}$ . However, directly regressing  $\mathbf{K}_i$  and  $\pi_i$  from the camera queries ( $\mathbf{Q}_{\text{cam}_i} \in \mathbb{R}^{N \times D}$  for the  $i$ -th view), which entails regressing only 16 parameters (9 for the rotation matrix, 3 for translation, and 4 for intrinsics including focal lengths and principal points) from the  $N \times D$  parameters through an MLP, may be suboptimal for neural learning Zhang et al. (2024c). Therefore, inspired by Zhang et al. (2024c), we represent the camera parameters by  $N$  rays, transferring starting from the camera center to the  $N$  2D reference points on the image plane as shown in Fig. 3. More specifically, our approach over-parameterize camera in the  $i$ -th view by a set of rays  $\mathcal{R}_i = \mathbf{r}_{i1}, \dots, \mathbf{r}_{iN}$ , where each ray  $\mathbf{r}_{ij} \in \mathbb{R}^6$  is represented by Plücker coordinates (Plücker, 1828):  $\mathbf{r}_{ij} \in \mathbb{R}^6$ . Different from previous methods (Zhang et al., 2024c), we define the rays sparsely on the 2D reference points instead of on each pixel to enhance the relationship between 3D Gaussians and camera parameters. After each layer, once the rays are predicted by Eq. (3), the camera parameters can be solved by RQ-decomposition on an overdetermined system of equations from the Plücker coordinates of RefRay with details of Plücker-camera sparse mapping in Appendix A.2.

### 3.5 Training objective

We leverage the differentiable rendering method 3D GS Kerbl et al. (2023) to generate RGB images from the 3D Gaussians  $\mathbf{G}$  predicted by our model. Aligning with Hong et al. (2024c); Tang et al. (2024); Ye et al. (2025), we employ an RGB loss in Eq. (10), which consists of both a mean square error loss  $\mathcal{L}_{\text{MSE}}$  and a VGG-based LPIPS (Learned Perceptual Image Patch Similarity) loss (Zhang et al., 2018a)  $\mathcal{L}_{\text{LPIPS}}$ , to guide the rendered views. Here  $I_{pd}$  and  $I_{gt}$  represent rendered views and ground truth images, respectively.

$$\mathcal{L}_{3D} = \mathcal{L}_{\text{MSE}}(I_{pd}, I_{gt}) + \lambda \mathcal{L}_{\text{LPIPS}}(I_{pd}, I_{gt}) \quad (10)$$

For the camera parameters, with the 2D reference points, we can calculate the rays from the ground truth camera center to the  $N$  2D reference points to get the ray supervision  $\mathcal{R}_{j_{gt}}$ . The ray loss is defined as Eq. (11).

$$\mathcal{L}_{\text{rays}} = \sum_{j=1}^N \|\mathcal{R}_{j_{gt}} - \mathcal{R}_{j_{pd}}\|_2. \quad (11)$$

The total loss can be described as Eq. (12), where  $\lambda_{\text{rays}}$  and  $\lambda_{3D}$  are weights of 3D and ray loss, respectively.

$$\mathcal{L} = \lambda_{\text{rays}} \mathcal{L}_{\text{rays}} + \lambda_{3D} \mathcal{L}_{3D} \quad (12)$$



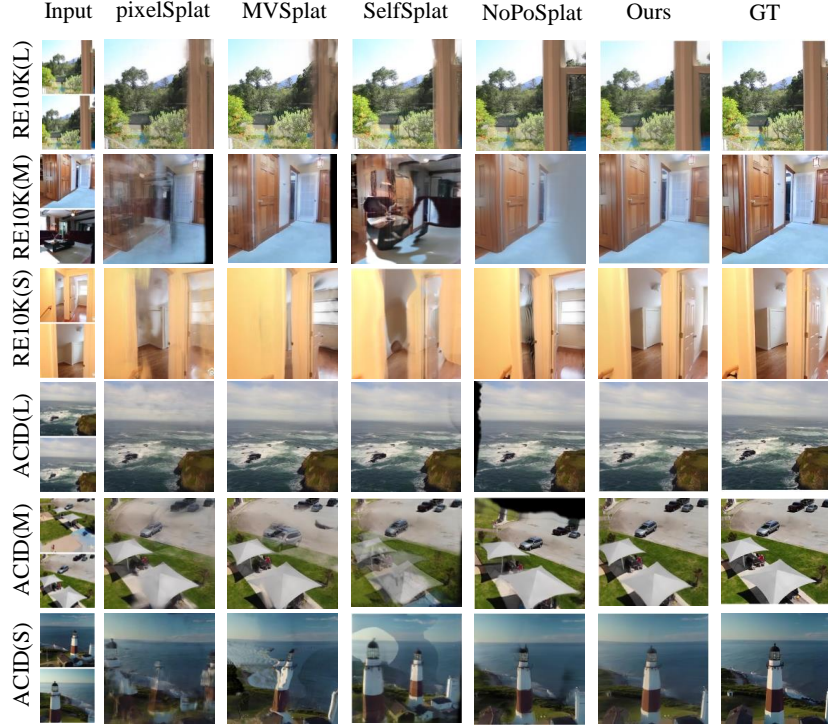


**Figure 4:** Qualitative comparison on RE10K and ACID datasets. the ‘L’, ‘M’, and ‘S’ in the brackets meaning the groups of overlapping large, medium, and small, respectively.

## 4 Experiments

Table 2: Novel view synthesis performance comparison on the ACID (Liu et al., 2021) dataset. ‘-A’ means with evaluation-time pose alignment.

Method	Overlap Settings								
	Small			Medium			Large		
	PSNR↑	SSIM↑	LPIPS↓	PSNR↑	SSIM↑	LPIPS↓	PSNR↑	SSIM↑	LPIPS↓
<b>Pose-Required</b>									
pixelNeRF	19.376	0.535	0.564	20.339	0.561	0.537	20.826	0.576	0.509
AttnRend	20.942	0.616	0.398	24.004	0.720	0.301	27.117	0.808	0.207
pixelSplat	22.053	0.654	0.285	25.460	0.776	0.198	28.426	0.853	0.140
MVsplat	21.392	0.639	0.290	25.103	0.770	0.199	28.388	0.852	0.139
<b>Pose-Free</b>									
DUSi3R	14.494	0.372	0.502	16.256	0.411	0.453	17.324	0.431	0.408
MASt3R	14.242	0.366	0.522	16.169	0.411	0.463	17.270	0.430	0.423
CoPoNeRF	18.651	0.551	0.485	20.654	0.595	0.418	22.654	0.652	0.343
NoPoSplat	21.987	0.603	0.278	23.236	0.689	0.238	24.468	0.746	0.180
NoPoSplat-A	23.087	0.685	0.258	25.624	0.777	0.193	28.043	0.841	0.144
Ours	22.809	0.658	0.228	23.292	0.707	0.218	24.625	0.783	0.172
<b>Ours-A</b>	<b>24.343</b>	<b>0.713</b>	<b>0.237</b>	<b>25.933</b>	<b>0.798</b>	<b>0.187</b>	<b>28.467</b>	<b>0.859</b>	<b>0.120</b>
<b>Average</b>									
	20.323	0.561	0.533	24.475	0.730	0.287	25.819	0.779	0.195

**Datasets** Our paper focuses on benchmarking the Novel View Synthesis (NVS) task using the entire scene dataset. We have aligned our approach with the datasets employed in prior works Ye et al. (2025); Chen, Yuedong and Xu, Haofei and Zheng, Chuanxia and Zhuang, Bohan and Pollefeys, Marc and Geiger, Andreas and Cham, Tat-Jen and Cai, Jianfei (2024); Charatan et al. (2024), which leverage RealEstate10K (RE10K) (Zhou et al., 2018) and ACID (Liu et al., 2021) predominantly for both training and testing. We have adhered to the same train-test division and utilized the associated view indices outlined in Ye et al. (2025). Additionally, to enhance the scalability of our model, we have followed the approach in Ye et al. (2025) by incorporating the combined datasets of RE10K and DL3DV (Ling et al., 2024) (including all 11K subsets) for model training.



Table 3: Novel view synthesis performance comparison on the RealEstate10k (Zhou et al., 2018) dataset. ‘-A’ means with evaluation-time pose alignment. ‘-IF’ means the model is intrinsic free.

Method	Overlap Settings											
	Small			Medium			Large			Average		
	PSNR↑	SSIM↑	LPIPS↓	PSNR↑	SSIM↑	LPIPS↓	PSNR↑	SSIM↑	LPIPS↓	PSNR↑	SSIM↑	LPIPS↓
<b>Pose-Required</b>												
pixelNeRF	18.417	0.601	0.526	19.930	0.632	0.458	20.869	0.639	0.485	19.824	0.626	0.485
AttnRend	19.151	0.663	0.368	22.532	0.763	0.186	25.897	0.845	0.269	22.664	0.762	0.269
pixelSplat	20.263	0.717	0.266	23.711	0.809	0.181	27.151	0.879	0.122	23.848	0.806	0.185
MVSplat	20.353	0.724	0.250	23.778	0.812	0.173	27.408	0.884	0.116	23.977	0.811	0.176
<b>Pose-Free</b>												
DUST3R	14.101	0.432	0.468	15.419	0.451	0.402	16.427	0.453	0.432	15.382	0.447	0.432
MASt3R	13.534	0.407	0.494	14.945	0.436	0.418	16.028	0.444	0.452	14.907	0.431	0.452
Splatt3R	14.352	0.475	0.472	15.529	0.502	0.425	15.817	0.483	0.421	15.318	0.490	0.436
CoPoNeRF	17.393	0.585	0.462	18.813	0.616	0.392	20.464	0.652	0.318	18.938	0.619	0.388
SelfSplat	17.506	0.550	0.461	19.357	0.704	0.378	20.868	0.672	0.256	19.33	0.656	0.363
NoPoSplat	21.814	0.765	0.220	23.044	0.787	0.178	25.408	0.844	0.126	23.424	0.798	0.173
NoPoSplat-A	22.514	0.784	0.210	24.899	0.839	0.160	27.411	0.883	0.119	25.033	0.838	0.160
Ours-IF	21.312	0.741	0.234	22.891	0.773	0.189	25.312	0.829	0.138	23.200	0.781	0.185
Ours	22.843	0.781	0.192	23.394	0.804	0.175	26.270	0.872	0.110	24.093	0.818	0.160
<b>Ours-A</b>	<b>24.117</b>	<b>0.827</b>	<b>0.177</b>	<b>25.018</b>	<b>0.859</b>	<b>0.159</b>	<b>27.985</b>	<b>0.904</b>	<b>0.110</b>	<b>25.656</b>	<b>0.864</b>	<b>0.149</b>

**Evaluation metrics** Our model optimizes pose-free NVS and pose estimation simultaneously. For NVS evaluation, we consider metrics such as PSNR, SSIM, and LPIPS (Zhang et al., 2018b). In terms of pose estimation, we calculate the Area Under the Curve (AUC) for cumulative pose error using thresholds of  $5^\circ$ ,  $10^\circ$ , and  $20^\circ$  (Ye et al., 2025; Sarlin et al., 2020). Furthermore, we also evaluate the performance of our model using input views with varying degrees of overlap, where a larger overlap indicates closer proximity between the input views. We categorize the overlaps into three groups: small (5% - 30%), medium (30% - 55%), and large (55% - 80%) following (Ye et al., 2025).

**Baselines** We conduct comparison to the pose-free method NoPoSplat (Ye et al., 2025), and also other sparse view reconstruction methods, including pose-required methods pixelNeRF (Yu et al., 2021), AttnRend (Du et al., 2023), pixelSplat (Charatan et al., 2024), and MVSplat (Chen, Yuedong and Xu, Haoifei and Zheng, Chuanxia and Zhuang, Bohan and Pollefeys, Marc and Geiger, Andreas and Cham, Tat-Jen and Cai, Jianfei, 2024), and pose-free methods DUST3R (Wang et al., 2024), MASt3R (Leroy et al., 2024), Splatt3R (Smart et al., 2024), SelfSplat (Kang et al., 2024), CoPoNeRF (Hong et al., 2023), and RoMa (Edstedt et al., 2024).

**Implementation details** We employ ViT initialized by NoPoSplat and multi-layer refinement contains 4 layers. In accordance with prior research, we input all images at a resolution of  $256 \times 256$ . To compare fairly, we select the number of 3D Gaussians being same to previous methods, that is, the number of pixels in 2 views ( $2 \times 256 \times 256$ ). Our model is trained on 8 A100 GPUs for 1 day.

## 4.1 Results and analysis

**Quantity results for NVS** The comparison results for NVS performance on RE10K and ACID dataset are depicted in Table 3 and Table 2. As demonstrated in the table, our model consistently outperforms previous methods, even surpassing methods that rely on ground-truth pose input, particularly excelling in scenarios with limited view overlap. In particular, our unposed image model successfully reconstructs a plausible 3D scene that aligns well with the inputs provided. However, reconstructing a 3D scene with only two input views inherently poses challenges due to the ambiguity arising from multiple scenes producing the same pair of images (Ye et al., 2025). To address this, as discussed in Ye et al. (2025); Fan et al. (2024); Wang et al. (2021), we adopt an evaluation-time pose alignment strategy to refine the camera pose for the target view, ensuring a fair comparison. For each evaluation sample, we initially reconstruct 3D Gaussians using our proposed approach. Subsequently, we fine-tune the target camera pose to align the rendered image closely with the ground-truth image. We present results for both models with and without this alignment, denoting the aligned method with ‘-A’. As outlined in Section 3.4, rays are capable of representing not only camera poses but also intrinsics. Consequently, we conduct experiments that do not provide intrinsics but instead predicted them, the results are represented by ‘Ours-IF’ in Table 3. The results is worse than using ground-truth intrinsics but comparable to previous methods.

**Quality results for NVS** We present quality comparisons with pose-required methods (pixelSplat (Charatan et al., 2024) and MVSplat (Chen, Yuedong and Xu, Haoifei and Zheng, Chuanxia and Zhuang, Bohan and Pollefeys, Marc and Geiger, Andreas and Cham, Tat-Jen and Cai, Jianfei, 2024)) and the two categories of pose-free methods mentioned in Section 1. The first category is that solely optimize 3D while neglecting poses (NoPoSplat (Ye et al., 2025)) and the second category is that optimize both pose and 3D using separate networks (SelfSplat (Kang et al., 2024)) Fig. 4 and Appendix A.6. Our method demonstrates superior performance compared to previous ones. Pose-required methods typically employ a ‘transform-then-fuse’ strategy (Ye et al., 2025), generating 3D Gaussians under each view’s camera coordinates and then concatenating them in world coordinates, resulting in blurring in novel views. Pose-free methods that focus solely on 3D may encounter issues with incorrect rendering in novel views due to improper pose handling. Pose-free methods that optimize 3D and pose separately risk inaccurate novel views resulting from improper pose estimations.

**Relative pose estimation** The results of relative pose estimated are presented in Table 4. Aligning with Ye et al. (2025), we assess the performance in pose estimation by training two models in different datasets. One model is trained using the RE10K dataset, while the other is trained using a combination of RE10K and DL3DV datasets, denoted as ‘Ours’ and ‘Ours\*’ in the table, respectively. We evaluate the performance on both the RE10K test set and the ACID test set to demonstrate the efficacy of our models on both in-domain and cross-domain datasets. The results indicate that as the training set grows, the accuracy of pose estimation improves. The comparison on another evaluation matrix with rotation and translation error is shown in Table 8.

Table 4: Pose estimation performance in AUC with various thresholds on RE10k, ACID. Methods with ‘\*’ meaning the model is trained on RE10k+DL3DV dataset, otherwise only on RE10K. ‘-A’ means with evaluation-time pose alignment.

Method	RE10k			ACID		
	5° ↑	10° ↑	20° ↑	5° ↑	10° ↑	20° ↑
CoPoNeRF	0.161	0.362	0.575	0.078	0.216	0.398
DUST3R	0.301	0.495	0.657	0.166	0.304	0.437
MASt3R	0.372	0.561	0.709	0.234	0.396	0.541
RoMa	0.546	0.698	0.797	0.463	0.588	0.689
NoPoSplat	0.546	0.719	0.843	0.366	0.519	0.654
NoPoSplat*	0.623	0.775	0.867	0.440	0.578	0.693
NoPoSplat-A	0.672	0.792	0.869	0.454	0.591	0.709
NoPoSplat-A*	0.691	0.806	0.877	0.486	0.617	0.728
Ours	0.605	0.749	0.885	0.405	0.556	0.661
Ours*	0.650	0.788	0.887	0.451	0.587	0.702
Ours-A	0.710	0.805	0.887	0.487	0.610	0.715
Ours-A*	0.683	0.810	0.886	0.499	0.627	0.735

**Geometry reconstruction** To conduct a comprehensive comparison between our model and previous approaches based on the reconstructed 3D Gaussians rather than solely novel views, we present the rendered geometry depicted using 3D Gaussians in Fig. 5. The results of geometry are visualized by the code provided by Charatan et al. (2024); Chen, Yuedong and Xu, Haoifei and Zheng, Chuanxia and Zhuang, Bohan and Pollefeys, Marc and Geiger, Andreas and Cham, Tat-Jen and Cai, Jianfei (2024). As illustrated in the figure, by jointly optimizing 3D Gaussians and input view camera poses, our methods achieve better alignment between input views, resulting in reduced artifacts within the reconstructed scenes. Furthermore, our model exhibits enhanced performance in reconstructing missing elements that were challenging for previous methods.

**Model Efficiency** To show the model efficiency of our model, we test the inference time on a 3090 GPU with batch size 1. As shown in Table 5, our method can predict 3D Gaussians together with the camera poses from two  $256 \times 256$  input images in 0.131 seconds (7.63 fps), outperforms previous methods.

**In-the-wild input images** To ensure that our model can generalize beyond the training dataset, we evaluated it on in-the-wild images, as illustrated in Fig. 6. Our model demonstrates ability in both indoor and outdoor scenes.

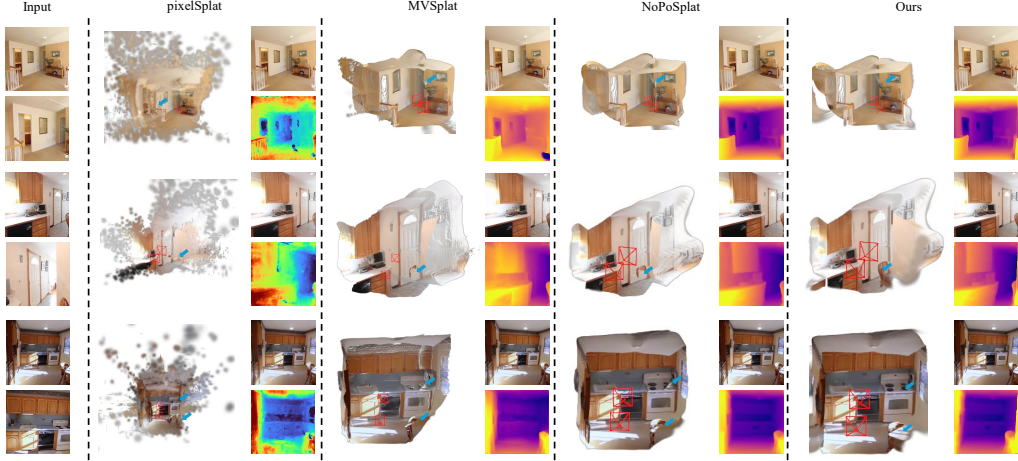


**Figure 5:** Geometry visualization with renderd novel view and depth. Our model demonstrates enhanced performance in addressing specific artifacts in the first row. Furthermore, our model excels in reconstructing missing elements that were challenging for prior approaches, (like chairs and tables situated in the corner), indicated by the blue arrows.

Table 5: Inference time comparison. ‘3D time’ denotes the duration for reconstructing 3D scenes, ‘pose time’ signifies the time taken for pose estimation, ‘forward time’ represents the total duration for inferring both 3D scenes and poses, while ‘rendering time’ indicates the time for NVS from 3D for a single image. For the network without the parts or has no separate parts, we use ‘NA’. without All measurements are in seconds.

Method	3D time	Pose time	Forward time	Rendering time
pixelSplat	0.825	NA	0.825	<b>0.003</b>
MVsplat	0.0.301	NA	0.301	<b>0.003</b>
DBARF	NA	NA	1.132	1.268
DUST3R	0.062	0.211	0.273	<b>0.003</b>
MASt3R	0.079	0.211	0.290	<b>0.003</b>
NoPoSplat	0.108	0.211	0.319	<b>0.003</b>
Our model	NA	NA	<b>0.131</b>	<b>0.003</b>

## 4.2 Ablation studies

**Ground-truth pose input** In contrast to earlier pose-free methods lacking pose incorporation in their networks, our model optimizes 3D and pose jointly. Consequently, we can use the ground-truth poses as input to further enhance our model’s performance give they are given. By utilizing ground-truth pose data, our model demonstrates even better outcomes, as evidenced in Table 6.

**No CaMDFA** To demonstrate the significance of our custom CaMDFA decoder, we conducted an ablation study by omitting this component. In other words, we attempted to regress 3D Gaussians directly from the ViT encoder. The absence of the CaMDFA resulted in a decrease in performance as shown in Table 6.

**Regress camera pose as 6D pose** As discussed in Section 3.4, directly regressing 6D pose of the camera from queries with numerous parameters, leads to suboptimal results. To support this, we conducted an ablation study on directly regressing the 6D pose (rotation and translation) as shown in Table 6, with the results supporting our assertion.

**Rays on pixel** In our model, we define rays from the camera center to 2D reference points, which differs from the approach in Zhang et al. (2024c), where rays are defined from the camera center to each pixel or patch on the image. To demonstrate the effectiveness of our approach, we conduct an ablation study on the rays defined in Zhang et al. (2024c), referred to as ‘Rays on pixel’ in Table 6. As illustrated in the table, the design of our RefRay contributes to improved model performance.

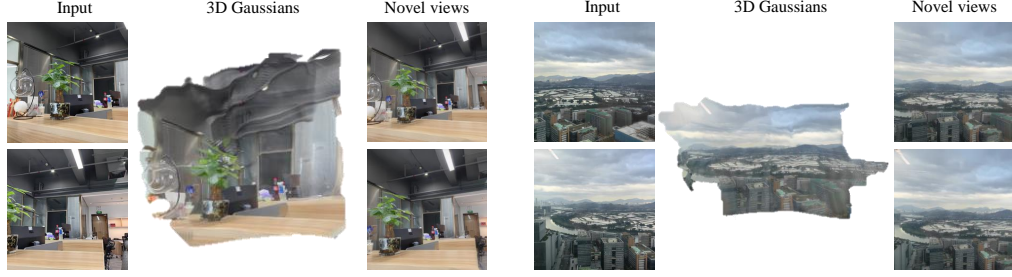


**Figure 6:** In-the-wild input images. Our method is applied using real-world photographs taken with mobile phones, encompassing both indoor and outdoor scenarios.

**Input more views** Our model is flexible and can receive an arbitrary number of input views rather than only two views. The inclusion of three input views yields superior results compared to two views, as demonstrated in Table 6. Additionally, we present the PSNR results for a larger number of input views, extending up to 10 views, in the model details section (Appendix A.6 Fig. 8).

Table 6: Ablation Studies on RE10K dataset.

Method	PSNR $\uparrow$	SSIM $\uparrow$	LPIPS $\downarrow$
Full model	25.656	0.864	0.149
GT pose input	26.217	0.870	0.138
No CaMDFA	23.916	0.808	0.172
6D pose	23.929	0.814	0.163
Rays on pixel	24.323	0.822	0.158
Input 3 views	26.706	0.884	0.124

**Number of Gaussians** We evaluate our model using the same number of 3D Gaussians as previous methods, equivalent to the total pixels in two input views (131,072). However, our model offers the flexibility to treat the number of 3D Gaussians as a hyperparameter. In our ablation study on the number of 3D Gaussians (Appendix A.6 Fig. 9), we observe that performance improves with an increased number of 3D Gaussians utilized.

## 5 Conclusion and Limitation

In conclusion, we introduce a novel approach **Coca-Splat** to optimizing 3D Gaussians and camera poses collaboratively within a unified network, enhancing the relationship between them for improved scene reconstruction and novel view synthesis. Inspired by Deformable DETR, our model represents define separate queries for 3D Gaussians and camera parameters, leveraging image features for efficient updates within **CaMDFA** block. This process involves projecting 3D queries onto image features using camera poses as 2D reference points and utilizing surrounding image features to update both 3D and camera queries. To tackle the challenge in regressing rotations and translations from numerous parameters, we adopt a ray-based design (RefRay) that representing camera poses as rays from the camera center to the 2D reference points on the image feature. Our methodology surpasses previous approaches on benchmark datasets like RealEstate10K and ACID, demonstrating its effectiveness and potential for advancing scene reconstruction and novel view synthesis.

**Limitations** A limitation persists in that the training datasets seldom contain videos that capture the entire 360-degree scenes. Consequently, our model lack the ability on reconstruct the 360° scenes from one forward.

## References

- Jonathan T Barron, Ben Mildenhall, Matthew Tancik, Peter Hedman, Ricardo Martin-Brualla, and Pratul P Srinivasan. Mip-NeRF: A Multiscale Representation for Anti-Aliasing Neural Radiance Fields. In IEEE/CVF International Conference on Computer Vision (ICCV), 2021.
- Wenjing Bian, Zirui Wang, Kejie Li, Jia-Wang Bian, and Victor Adrian Prisacariu. NoPe-NeRF: Optimising Neural Radiance Field With No Pose Prior. In Proceedings of the IEEE/CVF Conference on Computer Vision and Pattern Recognition, pages 4160–4169, 2023.
- David Charatan, Sizhe Lester Li, Andrea Tagliasacchi, and Vincent Sitzmann. pixelsplat: 3d gaussian splats from image pairs for scalable generalizable 3d reconstruction. In Proceedings of the IEEE/CVF Conference on Computer Vision and Pattern Recognition, pages 19457–19467, 2024.
- Guikun Chen and Wenguan Wang. A Survey on 3D Gaussian Splatting. ArXiv, 2024.
- Yu Chen and Gim Hee Lee. DBARF: Deep Bundle-Adjusting Generalizable Neural Radiance Fields. In Proceedings of the IEEE/CVF Conference on Computer Vision and Pattern Recognition, pages 24–34, 2023.
- Chen, Yuedong and Xu, Haoifei and Zheng, Chuanxia and Zhuang, Bohan and Pollefeys, Marc and Geiger, Andreas and Cham, Tat-Jen and Cai, Jianfei. Mvsplat: Efficient 3d gaussian splatting from sparse multi-view images. European Conference on Computer Vision, 2024.
- Shin-Fang Chng, Sameera Ramasinghe, Jamie Sherrah, and Simon Lucey. Gaussian activated neural radiance fields for high fidelity reconstruction and pose estimation. In European Conference on Computer Vision, pages 264–280. Springer, 2022.
- Feng Dai, Yuan Xu, Feng Dai, and Yuan Xu. Spherical harmonics. Approximation theory and harmonic analysis on spheres and balls, pages 1–27, 2013.
- Alexey Dosovitskiy, Lucas Beyer, Alexander Kolesnikov, Dirk Weissenborn, Xiaohua Zhai, Thomas Unterthiner, Mostafa Dehghani, Matthias Minderer, Georg Heigold, Sylvain Gelly, et al. An Image is Worth 16x16 Words: Transformers for Image Recognition at Scale. ICLR, 2021.
- Yilun Du, Cameron Smith, Ayush Tewari, and Vincent Sitzmann. Learning to render novel views from wide-baseline stereo pairs. In Proceedings of the IEEE/CVF Conference on Computer Vision and Pattern Recognition, pages 4970–4980, 2023.
- Johan Edstedt, Qiyu Sun, Georg Bökman, Mårten Wadenbäck, and Michael Felsberg. RoMa: Robust dense feature matching. In Proceedings of the IEEE/CVF Conference on Computer Vision and Pattern Recognition, pages 19790–19800, 2024.
- Zhiwen Fan, Wenyan Cong, Kairun Wen, Kevin Wang, Jian Zhang, Xinghao Ding, Danfei Xu, Boris Ivanovic, Marco Pavone, Georgios Pavlakos, et al. InstantSplat: Unbounded sparse-view pose-free gaussian splatting in 40 seconds. arXiv preprint arXiv:2403.20309, 2(3):4, 2024.
- David A Forsyth and Jean Ponce. A Modern Approach. Computer vision: a modern approach, 17:21–48, 2003.
- Stephan J. Garbin, Marek Kowalski, Matthew Johnson, Jamie Shotton, and Julien P. C. Valentin. FastNeRF: High-Fidelity Neural Rendering at 200FPS. In IEEE/CVF International Conference on Computer Vision (ICCV), 2021.
- Richard Hartley and Andrew Zisserman. Multiple View Geometry in Computer Vision. Cambridge university press, 2003.
- R. Hartley and A. Zisserman. Multiple View Geometry in Computer Vision. Cambridge University Press, 2004.
- Sunghwan Hong, Jaewoo Jung, Heeseong Shin, Jiaolong Yang, Seungryong Kim, and Chong Luo. Unifying Correspondence, Pose and NeRF for Pose-Free Novel View Synthesis from Stereo Pairs. arXiv preprint arXiv:2312.07246, 2023.
- Sunghwan Hong, Jaewoo Jung, Heeseong Shin, Jisang Han, Jiaolong Yang, Chong Luo, and Seungryong Kim. PF3plat: Pose-Free Feed-Forward 3D Gaussian Splatting. arXiv preprint arXiv:2410.22128, 2024a.
- Sunghwan Hong, Jaewoo Jung, Heeseong Shin, Jiaolong Yang, Seungryong Kim, and Chong Luo. Unifying Correspondence, Pose and NeRF for Pose-Free Novel View Synthesis from Stereo Pairs. CVPR, 2024b.
- Yicong Hong, Kai Zhang, Jiuxiang Gu, Sai Bi, Yang Zhou, Difan Liu, Feng Liu, Kalyan Sunkavalli, Trung Bui, and Hao Tan. LRM: Large Reconstruction Model for Single Image to 3D. In International Conference on Learning Representations (ICLR), 2024c.

- Hanwen Jiang, Zhenyu Jiang, Yue Zhao, and Qixing Huang. Leap: Liberate sparse-view 3d modeling from camera poses. arXiv preprint arXiv:2310.01410, 2023.
- Hanwen Jiang, Zhenyu Jiang, Kristen Grauman, and Yuke Zhu. Few-View Object Reconstruction with Unknown Categories and Camera Poses. In 2024 International Conference on 3D Vision (3DV), pages 31–41. IEEE, 2024.
- Gyeongjin Kang, Jisang Yoo, Jiyeon Park, Seungtae Nam, Hyeonsoo Im, Sangpil Kim, Eunbyung Park, et al. SelfSplat: Pose-Free and 3D Prior-Free Generalizable 3D Gaussian Splatting. arXiv preprint arXiv:2411.17190, 2024.
- Tero Karras, Samuli Laine, and Timo Aila. A Style-Based Generator Architecture for Generative Adversarial Networks. In Proceedings of the IEEE/CVF conference on computer vision and pattern recognition (CVPR), pages 4401–4410, 2019.
- Tero Karras, Samuli Laine, Miika Aittala, Janne Hellsten, Jaakko Lehtinen, and Timo Aila. Analyzing and Improving the Image Quality of StyleGAN. In Proceedings of the IEEE/CVF conference on computer vision and pattern recognition (CVPR), pages 8110–8119, 2020.
- Bernhard Kerbl, Georgios Kopanas, Thomas Leimkuehler, and George Drettakis. 3D Gaussian Splatting for Real-Time Radiance Field Rendering. In ACM Transactions on Graphics (TOG), 2023.
- Akshay Krishnan, Abhijit Kundu, Kevis-Kokitsi Maninis, James Hays, and Matthew Brown. OmniNOCS: A unified NOCS dataset and model for 3D lifting of 2D objects. In European Conference on Computer Vision, pages 127–145. Springer, 2024.
- Vincent Leroy, Yohann Cabon, and Jérôme Revaud. Grounding image matching in 3d with mast3r. In European Conference on Computer Vision, pages 71–91. Springer, 2024.
- Jiahao Li, Hao Tan, Kai Zhang, Zexiang Xu, Fujun Luan, Yinghao Xu, Yicong Hong, Kalyan Sunkavalli, Greg Shakhnarovich, and Sai Bi. Instant3D: Fast Text-to-3D with Sparse-View Generation and Large Reconstruction Model. The International Conference on Learning Representations (ICLR), 2023.
- Amy Lin, Jason Y Zhang, Deva Ramanan, and Shubham Tulsiani. Relpose++: Recovering 6d poses from sparse-view observations. In 2024 International Conference on 3D Vision (3DV), pages 106–115. IEEE, 2024.
- Lu Ling, Yichen Sheng, Zhi Tu, Wentian Zhao, Cheng Xin, Kun Wan, Lantao Yu, Qianyu Guo, Zixun Yu, Yawen Lu, et al. D13dv-10k: A large-scale scene dataset for deep learning-based 3d vision. In Proceedings of the IEEE/CVF Conference on Computer Vision and Pattern Recognition, pages 22160–22169, 2024.
- Andrew Liu, Richard Tucker, Varun Jampani, Ameesh Makadia, Noah Snively, and Angjoo Kanazawa. Infinite Nature: Perpetual View Generation of Natural Scenes from a Single Image. In Proceedings of the IEEE/CVF International Conference on Computer Vision (ICCV), 2021.
- Changkun Liu, Shuai Chen, Yash Bhargat, Siyan Hu, Ming Cheng, Zirui Wang, Victor Adrian Prisacariu, and Tristan Braud. GS-CPR: Efficient Camera Pose Refinement via 3D Gaussian Splatting. arXiv preprint arXiv:2408.11085, 2024a.
- Fangfu Liu, Wenqiang Sun, Hanyang Wang, Yikai Wang, Haowen Sun, Junliang Ye, Jun Zhang, and Yueqi Duan. Reconx: Reconstruct any scene from sparse views with video diffusion model. arXiv preprint arXiv:2408.16767, 2024b.
- Xiaoxiao Long, Yuan-Chen Guo, Cheng Lin, Yuan Liu, Zhiyang Dou, Lingjie Liu, Yuexin Ma, Song-Hai Zhang, Marc Habermann, Christian Theobalt, et al. Wonder3d: Single image to 3d using cross-domain diffusion. In Proceedings of the IEEE/CVF Conference on Computer Vision and Pattern Recognition, pages 9970–9980, 2024.
- Hideobu Matsuki, Riku Murai, Paul HJ Kelly, and Andrew J Davison. Gaussian Splatting Slam. In Proceedings of the IEEE/CVF Conference on Computer Vision and Pattern Recognition, pages 18039–18048, 2024.
- Ben Mildenhall, Pratul P. Srinivasan, Matthew Tancik, Jonathan T. Barron, Ravi Ramamoorthi, and Ren Ng. NeRF: Representing Scenes as Neural Radiance Fields for View Synthesis. In The European Conference on Computer Vision (ECCV), 2020.
- Thomas Müller, Alex Evans, Christoph Schied, and Alexander Keller. Instant Neural Graphics Primitives with a Multiresolution Hash Encoding. In ACM Transactions on Graphics (SIGGRAPH), 2022.
- Julius Plücker. Analytisch-geometrische Entwicklungen. GD Baedeker, 1828.

- Charles R Qi, Hao Su, Kaichun Mo, and Leonidas J Guibas. PointNet: Deep Learning on Point Sets for 3D Classification and Segmentation. In Proceedings of the IEEE conference on computer vision and pattern recognition (CVPR), pages 652–660, 2017.
- Marie-Julie Rakotosaona, Fabian Manhardt, Diego Martin Arroyo, Michael Niemeyer, Abhijit Kundu, and Federico Tombari. NeRFMeshing: Distilling Neural Radiance Fields into Geometrically-Accurate 3D Meshes. In International Conference on 3D Vision (3DV), 2023.
- Robin Rombach, Andreas Blattmann, Dominik Lorenz, Patrick Esser, and Björn Ommer. High-resolution image synthesis with latent diffusion models. In Proceedings of the IEEE/CVF conference on computer vision and pattern recognition (CVPR), pages 10684–10695, 2022.
- Mehdi S. M. Sajjadi, Henning Meyer, Etienne Pot, Urs Bergmann, Klaus Greff, Noha Radwan, Suhani Vora, Mario Lucic, Daniel Duckworth, Alexey Dosovitskiy, Jakob Uszkoreit, Thomas Funkhouser, and Andrea Tagliasacchi. Scene Representation Transformer: Geometry-Free Novel View Synthesis Through Set-Latent Scene Representations. CVPR, 2022.
- Paul-Edouard Sarlin, Daniel DeTone, Tomasz Malisiewicz, and Andrew Rabinovich. SuperGlue: Learning Feature Matching with Graph Neural Networks. In Proceedings of the IEEE/CVF conference on computer vision and pattern recognition, pages 4938–4947, 2020.
- Johannes L. Schonberger and Jan-Michael Frahm. Structure-From-Motion Revisited. In Proceedings of the IEEE Conference on Computer Vision and Pattern Recognition (CVPR), 2016.
- Yichun Shi, Peng Wang, Jianglong Ye, Long Mai, Kejie Li, and Xiao Yang. MVDream: Multi-view Diffusion for 3D Generation. The International Conference on Learning Representations (ICLR), 2024.
- Brandon Smart, Chuanxia Zheng, Iro Laina, and Victor Adrian Prisacariu. Splatt3r: Zero-shot gaussian splatting from uncalibrated image pairs. arXiv preprint arXiv:2408.13912, 2024.
- Cameron Smith, Yilun Du, Ayush Tewari, and Vincent Sitzmann. FlowCam: Training Generalizable 3D Radiance Fields without Camera Poses via Pixel-Aligned Scene Flow. NeurIPS, 2023.
- N. Snavely, S. M. Seitz, and R. Szeliski. Photo Tourism: Exploring Photo Collections in 3D. In ACM Transactions on Graphics (TOG), pages 835–846, 2006.
- Jiaxiang Tang, Zhaoxi Chen, Xiaokang Chen, Tengfei Wang, Gang Zeng, and Ziwei Liu. LGM: Large Multi-View Gaussian Model for High-Resolution 3D Content Creation. In European Conference on Computer Vision, pages 1–18. Springer, 2024.
- Yuri Viazovetskyi, Vladimir Ivashkin, and Evgeny Kashin. StyleGAN2 Distillation for Feed-forward Image Manipulation. In Proceedings of the IEEE/CVF European Conference on Computer Vision (ECCV), pages 170–186. Springer, 2020.
- He Wang, Srinath Sridhar, Jingwei Huang, Julien Valentin, Shuran Song, and Leonidas J Guibas. Normalized Object Coordinate Space for Category-Level 6D Object Pose and Size Estimation. In Proceedings of the IEEE/CVF conference on computer vision and pattern recognition, pages 2642–2651, 2019.
- Jianyuan Wang, Christian Rupprecht, and David Novotny. PoseDiffusion: Solving Pose Estimation via Diffusion-aided Bundle Adjustment. In Proceedings of the IEEE/CVF International Conference on Computer Vision, pages 9773–9783, 2023a.
- Peng Wang and Yichun Shi. ImageDream: Image-Prompt Multi-view Diffusion for 3D Generation. arXiv preprint arXiv:2312.02201, 2023.
- Peng Wang, Hao Tan, Sai Bi, Yinghao Xu, Fujun Luan, Kalyan Sunkavalli, Wenping Wang, Zexiang Xu, and Kai Zhang. PF-LRM: Pose-Free Large Reconstruction Model for Joint Pose and Shape Prediction. arXiv preprint arXiv:2311.12024, 2023b.
- Shuzhe Wang, Vincent Leroy, Yohann Cabon, Boris Chidlovskii, and Jerome Revaud. Dust3r: Geometric 3d vision made easy. In Proceedings of the IEEE/CVF Conference on Computer Vision and Pattern Recognition, pages 20697–20709, 2024.
- Zirui Wang, Shangzhe Wu, Weidi Xie, Min Chen, and Victor Adrian Prisacariu. NeRF-: Neural radiance fields without known camera parameters. arXiv preprint arXiv:2102.07064, 2021.
- Bowen Wen, Jonathan Tremblay, Valts Blukis, Stephen Tyree, Thomas Müller, Alex Evans, Dieter Fox, Jan Kautz, and Stan Birchfield. BundleSDF: Neural 6-DoF Tracking and 3D Reconstruction of Unknown Objects. In CVPR, 2023.



- Bowen Wen, Wei Yang, Jan Kautz, and Stan Birchfield. FoundationPose: Unified 6D Pose Estimation and Tracking of Novel Objects. In CVPR, 2024.
- Jiamin Wu, Kenkun Liu, Yukai Shi, Xiaoke Jiang, Yuan Yao, and Lei Zhang. UniG: Modelling Unitary 3D Gaussians for View-consistent 3D Reconstruction. arXiv preprint arXiv:2410.13195, 2024.
- Jiamin Wu, Kenkun Liu, Han Gao, Xiaoke Jiang, and Lei Zhang. LeanGaussian: Breaking Pixel or Point Cloud Correspondence in Modeling 3D Gaussians. Conference on Computer Vision and Pattern Recognition (CVPR), 2025.
- Chao Xu, Ang Li, Linghao Chen, Yulin Liu, Ruoxi Shi, Hao Su, and Minghua Liu. SpaRP: Fast 3D Object Reconstruction and Pose Estimation from Sparse Views. In European Conference on Computer Vision, pages 143–163. Springer, 2024a.
- Jiale Xu, Weihao Cheng, Yiming Gao, Xintao Wang, Shenghua Gao, and Ying Shan. InstantMesh: Efficient 3D Mesh Generation from a Single Image with Sparse-view Large Reconstruction Models. arXiv preprint arXiv:2404.07191, 2024b.
- Yinghao Xu, Zifan Shi, Wang Yifan, Sida Peng, Ceyuan Yang, Yujun Shen, and Wetzstein Gordon. GRM: Large Gaussian Reconstruction Model for Efficient 3D Reconstruction and Generation, author=Xu Yinghao and Shi Zifan and Yifan Wang and Chen Hansheng and Yang Ceyuan and Peng Sida and Shen Yujun and Wetzstein Gordon, 2024c.
- Lior Yariv, Jiatao Gu, Yoni Kasten, and Yaron Lipman. Volume rendering of neural implicit surfaces. In Conference on Neural Information Processing Systems (NIPS), 2021.
- Botao Ye, Sifei Liu, Haoifei Xu, Li Xueting, Marc Pollefeys, Ming-Hsuan Yang, and Peng Songyou. No Pose, No Problem: Surprisingly Simple 3D Gaussian Splats from Sparse Unposed Images. ICLR, 2025.
- Alex Yu, Vickie Ye, Matthew Tancik, and Angjoo Kanazawa. pixelNeRF: Neural Radiance Fields from One or Few Images. In IEEE/CVF Conference on Computer Vision and Pattern Recognition (CVPR), 2021.
- Zehao Yu, Anpei Chen, Binbin Huang, Torsten Sattler, and Andreas Geiger. Mip-splatting: Alias-free 3d gaussian splatting. In Proceedings of the IEEE/CVF Conference on Computer Vision and Pattern Recognition, pages 19447–19456, 2024.
- Chubin Zhang, Hongliang Song, Yi Wei, Yu Chen, Jiwen Lu, and Yansong Tang. GeoLRM: Geometry-Aware Large Reconstruction Model for High-Quality 3D Gaussian Generation. NeurIPS, 2024a.
- Hao Zhang, Feng Li, Shilong Liu, Lei Zhang, Hang Su, Jun-Juan Zhu, Lionel Ming shuan Ni, and Heung yeung Shum. DINO: DETR with Improved DeNoising Anchor Boxes for End-to-End Object Detection. In The International Conference on Learning Representations (ICLR), 2023.
- Junyi Zhang, Charles Herrmann, Junhwa Hur, Varun Jampani, Trevor Darrell, Forrester Cole, Deqing Sun, and Ming-Hsuan Yang. MonST3R: A Simple Approach for Estimating Geometry in the Presence of Motion. arXiv preprint arXiv:2410.03825, 2024b.
- Jason Y Zhang, Deva Ramanan, and Shubham Tulsiani. Relpose: Predicting probabilistic relative rotation for single objects in the wild. In European Conference on Computer Vision, pages 592–611. Springer, 2022.
- Jason Y Zhang, Amy Lin, Moneish Kumar, Tzu-Hsuan Yang, Deva Ramanan, and Shubham Tulsiani. Cameras as Rays: Pose Estimation via Ray Diffusion. In International Conference on Learning Representations (ICLR), 2024c.
- Kai Zhang, Gernot Riegler, Noah Snavely, and Vladlen Koltun. NeRF++: Analyzing and Improving Neural Radiance Fields. ArXiv, 2020.
- Kai Zhang, Sai Bi, Hao Tan, Yuanbo Xiangli, Nanxuan Zhao, Kalyan Sunkavalli, and Zexiang Xu. GS-LRM: Large Reconstruction Model for 3D Gaussian Splatting. European Conference on Computer Vision, 2024d.
- Richard Zhang, Phillip Isola, Alexei A. Efros, Eli Shechtman, and Oliver Wang. The Unreasonable Effectiveness of Deep Features as a Perceptual Metric. In IEEE/CVF Conference on Computer Vision and Pattern Recognition (CVPR), 2018a.
- Richard Zhang, Phillip Isola, Alexei A Efros, Eli Shechtman, and Oliver Wang. The Unreasonable Effectiveness of Deep Features as a Perceptual Metric. In Proceedings of the IEEE conference on computer vision and pattern recognition (CVPR), pages 586–595, 2018b.

- Tinghui Zhou, Richard Tucker, John Flynn, Graham Fyffe, and Noah Snavely. Stereo Magnification: Learning View Synthesis using Multiplane Images. ACM Transactions on Graphics (TOG), 2018.
- Xizhou Zhu, Weijie Su, Lewei Lu, Bin Li, Xiaogang Wang, and Jifeng Dai. Deformable DETR: Deformable Transformers for End-to-End Object Detection. In The International Conference on Learning Representations (ICLR), 2021.
- Zihan Zhu, Songyou Peng, Viktor Larsson, Weiwei Xu, Hujun Bao, Zhaopeng Cui, Martin R. Oswald, and Marc Pollefeys. NICE-SLAM: Neural Implicit Scalable Encoding for SLAM. In Proceedings of the IEEE/CVF Conference on Computer Vision and Pattern Recognition (CVPR), 2022.
- Zihan Zhu, Songyou Peng, Viktor Larsson, Zhaopeng Cui, Martin R Oswald, Andreas Geiger, and Marc Pollefeys. Nicer-slam: Neural Implicit Scene Encoding for RGB Slam. In 2024 International Conference on 3D Vision (3DV), pages 42–52. IEEE, 2024.
- Zi-Xin Zou, Zhipeng Yu, Yuan-Chen Guo, Yangguang Li, Ding Liang, Yan-Pei Cao, and Song-Hai Zhang. Triplane Meets Gaussian Splatting: Fast and Generalizable Single-View 3D Reconstruction with Transformers. In Proceedings of the IEEE/CVF Conference on Computer Vision and Pattern Recognition (CVPR), pages 10324–10335, 2024.
- M. Zwicker, H. Pfister, J. van Baar, and M. Gross. EWA volume splatting. In IEEE Visualization (IEEE VIS), 2001.

## A Appendix

### A.1 Model details

#### A.1.1 Comparison to previous methods

Table 7: Methods comparison: ‘Pose-Free’ means that the model is pose-free, ‘Jointly Opt.’ means that the model optimize camera and 3D jointly, ‘Cano. Space’ means that the model define 3D points in the canonical space for all views, ‘Intri.-Free’ means that the model does not require intrinsic input.

Method	Pose-Free	Jointly Opt.	Cano. Space	Intri.-Free
PixelNeRF	✗	✗	✗	✗
PixelSplat	✗	✗	✗	✗
MVSplat	✗	✗	✗	✗
DUS3R	✓	✗	✓	✗
MASt3R	✓	✗	✓	✗
CoPoNeRF	✓	✓	✓	✗
SelfSplat	✓	✗	✗	✗
NoPoSplat	✓	✗	✓	✗
Ours	✓	✓	✓	✓

We offer a comparison with various methods in Table 7. Our model is a pose-free approach that jointly optimizes pose and scene, operating within canonical space, and is free from intrinsic constraints.

### A.2 RefRay

Typically, camera for the  $i$ -th view is parameterized by extrinsics  $\pi_i$  (consisting of rotations  $\pi_{iR} \in SO(3)$  and translations  $\pi_{iT} \in \mathbb{R}^3$ ) and intrinsics  $\mathbf{K}_i \in \mathbb{R}^{3 \times 3}$ . However, directly regressing  $\mathbf{K}_i$  and  $\pi_i$  from the camera queries ( $\mathbf{Q}_{\text{cam}_i} \in \mathbb{R}^{N \times D}$  for the  $i$ -th view), which entails regressing only 16 parameters (9 for the rotation matrix, 3 for translation, and 4 for intrinsics including focal lengths and principal points) from the  $N \times D$  parameters through an MLP, may be suboptimal for neural learning Zhang et al. (2024c). Therefore, inspired by Zhang et al. (2024c), we represent the camera parameters by  $N$  rays, transferring starting from the camera center to the  $N$  2D reference points on the image plane as shown in Fig. 3. More specifically, our approach over-parameterize camera in the  $i$ -th view by a set of rays  $\mathcal{R}_i = \mathbf{r}_{i1}, \dots, \mathbf{r}_{iN}$ , where each ray  $\mathbf{r}_{ij} \in \mathbb{R}^6$  is represented by Plücker coordinates (Plücker, 1828):  $\mathbf{r}_{ij} \in \mathbb{R}^6$ . Different from previous methods (Zhang et al., 2024c), we define the rays sparsely on the 2D reference points instead of on each pixel to enhance the relationship between 3D Gaussians and camera parameters. After each layer, once the rays are predicted by Eq. (3), the camera parameters can be solved by RQ-decomposition on a overdetermined system of equations from the Plücker coordinates of RefRay with details of Plücker-camera sparse mapping as following. We give the mapping from cameras to rays in Theorem 1 and the mapping from rays to cameras in Theorem 2

**Theorem 1. Cameras to rays mapping.** Given camera center  $\mathbf{c} \in \mathbb{R}^3$ , rotation matrix  $\mathbf{R} \in \mathbb{R}^{3 \times 3}$ , translation  $\mathbf{t} \in \mathbb{R}^3$ , camera intrinsics  $\mathbf{K} \in \mathbb{R}^{3 \times 3}$ , and a point  $\mathbf{x} \in \mathbb{R}^3$  in 3D with coordinate. The Plücker coordinates  $\mathbf{d}, \mathbf{m}$  for a ray passing through points  $\mathbf{x}$  and  $\mathbf{c}$ , which defined as  $\mathbf{d} = \mathbf{x} - \mathbf{c}$ ,  $\mathbf{m} = \mathbf{c} \times \mathbf{d}$  can be derived by

$$\mathbf{d} = \mathbf{R}^T \mathbf{K}^{-1} \mathbf{u}, \mathbf{m} = (-\mathbf{R}^T \mathbf{t}) \times \mathbf{d} \quad (13)$$

*Proof.* Given  $\mathbf{x}_W, \mathbf{x}_C$  denote the coordinates of point  $\mathbf{x}$  in world and camera coordinates and camera coordinates,  $\mathbf{c}_W, \mathbf{c}_C$  denote the coordinates of camera center  $\mathbf{c}$  in world and camera coordinates and camera coordinates. Let  $\mathbf{u}$  denotes the UV coordinates that derived from projecting  $\mathbf{x}$  to the image by camera parameters  $\mathbf{u} = \mathbf{K}(\mathbf{R}\mathbf{x}_W + \mathbf{t})$ .

$$\mathbf{c}_C = \mathbf{R}\mathbf{c}_W + \mathbf{t} \quad (14)$$

$$0 = \mathbf{R}\mathbf{c}_W + \mathbf{t} \quad (15)$$

$$\Rightarrow \mathbf{c}_W = -\mathbf{R}^T \mathbf{t} \quad (16)$$

$$\mathbf{x}_C = \mathbf{R}\mathbf{x}_W + \mathbf{t} \quad (17)$$

$$\mathbf{K}^{-1}\mathbf{u} = \mathbf{x}_C = \mathbf{R}\mathbf{x}_W + \mathbf{t} \quad (18)$$

$$\mathbf{x}_W = \mathbf{R}^T(\mathbf{K}^{-1}\mathbf{u} - \mathbf{t}) \quad (19)$$

$$= \mathbf{R}^T \mathbf{K}^{-1} \mathbf{u} - \mathbf{c}_C \quad (20)$$

Then use the definition of  $\mathbf{d}, \mathbf{m}$ ,

$$\mathbf{d} = \mathbf{x}_W - \mathbf{c}_W \quad (21)$$

$$= \mathbf{R}^T \mathbf{K}^{-1} \mathbf{u} \quad (22)$$

$$\mathbf{m} = \mathbf{c} \times \mathbf{d} \quad (23)$$

$$= (-\mathbf{R}^T \mathbf{t}) \times \mathbf{d} \quad (24)$$

□

**Theorem 2. Rays to cameras mapping.** Given a set of rays  $\mathcal{R} = \mathbf{r}_1, \dots, \mathbf{r}_N$ , which denote the  $N$  rays representing a camera with camera center  $\mathbf{c} \in \mathbb{R}^3$ , rotation matrix  $\mathbf{R} \in \mathbb{R}^{3 \times 3}$ , translation  $\mathbf{t} \in \mathbb{R}^3$ , camera intrinsics  $\mathbf{K} \in \mathbb{R}^{3 \times 3}$ , and projected points  $\mathbf{U}$  on the image plane from 3D points  $\mathbf{X}$ , the camera parameters can be solved by,

$$\mathbf{c} = \arg \min_{\mathbf{p} \in \mathbb{R}^3} \sum_{\langle \mathbf{d}, \mathbf{m} \rangle \in \mathcal{R}} |\mathbf{p} \times \mathbf{d} - \mathbf{m}|^2 \quad (25)$$

$$\mathbf{M} = \arg \min_{|\mathbf{H}|=1} \sum_{i=1}^m |\mathbf{H}\mathbf{d}_i \times \mathbf{u}_i| \quad (26)$$

where  $\mathbf{r} = \langle \mathbf{d}, \mathbf{m} \rangle \in \mathcal{R}$  denotes a ray passing through points  $\mathbf{x}$  and camera center  $\mathbf{c}$ ,  $\mathbf{d} = \mathbf{x} - \mathbf{c}$ ,  $\mathbf{m} = \mathbf{c} \times \mathbf{d}$ ,  $\mathbf{M} = \mathbf{K}\mathbf{R}$ .

*Proof.* All rays should passing through the same point  $\mathbf{c}$ , which is the camera center. In order to solve the camera center, we want

$$\mathbf{m} = \mathbf{c} \times \mathbf{d} \quad (27)$$

for all rays  $\mathbf{r} = \langle \mathbf{d}, \mathbf{m} \rangle \in \mathcal{R}$ . When the number of rays is greater than the the number of unknown parameters for camera center, this gives a overparameterized equation system.

$$\mathbf{c} = \arg \min_{\mathbf{p} \in \mathbb{R}^3} \sum_{\langle \mathbf{d}, \mathbf{m} \rangle \in \mathcal{R}} |\mathbf{p} \times \mathbf{d} - \mathbf{m}|^2 \quad (28)$$

As for the rotation matrix  $\mathbf{K}$  and intrinsics matrix  $\mathbf{K}$ , denoting  $\mathbf{M} = \mathbf{K}\mathbf{R}$ ,

$$\mathbf{d} = \mathbf{R}^T \mathbf{K}^{-1} \mathbf{u} \quad (29)$$

$$\Rightarrow \mathbf{K}\mathbf{R}\mathbf{d} = \mathbf{u} \quad (30)$$

$$\Rightarrow \mathbf{M}\mathbf{d} = \mathbf{u}. \quad (31)$$

Ignoring the translation here, we require the direction of  $\mathbf{M}\mathbf{d}$  and  $\mathbf{u}$  being the same, i.e.,

$$\mathbf{M}\mathbf{d} \times \mathbf{u} = 0. \quad (32)$$

Similar to what we do for camera center,  $\mathbf{M}$  can be solved by

$$\mathbf{M} = \arg \min_{|\mathbf{H}|=1} \sum_{i=1}^m |\mathbf{H}\mathbf{d}_i \times \mathbf{u}_i| \quad (33)$$

□

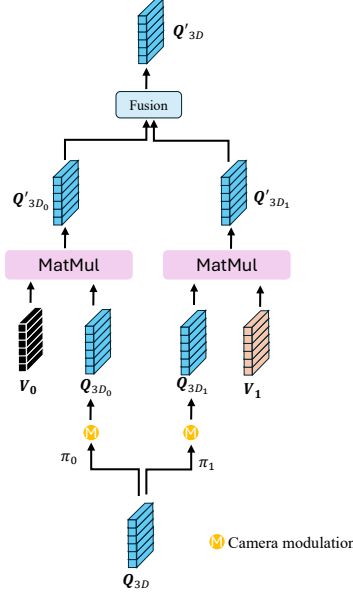


**Figure 7:** Query updation for CAMVDFA. The updating of queries for 3D Gaussians follows a similar process to that of camera queries. In this context, ‘MatMul’ signifies matrix multiplication.  $Q_{3D_i}$  stands for the 3D queries for the  $i$ -th input view, while  $Q'_{3D_i}$  indicates the updated 3D queries for the same view. Camera modulation has details in Section 3.3. Further insights into the fusion block, which combines the view-wise queries.

### A.3 Details for spatially efficient self-attention

Directly do self-attention on the 3D queries may cause large memory costs, particularly when  $N$  is extensive, we implement a spatially efficient self-attention strategy inspired by (Wu et al., 2024). This method involves sampling a subset of queries  $Q_{down}$  from  $Q_{3D}$  using the Fast Point Sampling (FPS) (Qi et al., 2017) algorithm on the locations of the queries, which are defined as the centers of 3D Gaussians. Such design focuses on 3D Gaussians positioned farthest apart and likely to encompass the entire scene. Keys and values are then derived from  $Q_{down}$  while queries are extracted from  $Q_{3D}$  by linear projection during self-attention computation. This approach minimizes memory consumption without compromising performance.

### A.4 Details for 3D queries initialization

3D queries are initialized by the flattening image features with shape  $V \times H \times W$ , where  $V$ ,  $H$ , and  $W$  represent the number of input views, height, and width of each view, respectively. Subsequently, the 3D queries are passed through  $Head_{3D}$  to initialize 3D Gaussians.

In cases where the resolution or the number of input views are large, resulting in large  $V \times H \times W$ , memory conservation becomes crucial. To address this, we introduce a hyperparameter  $N_{3D}$  to denote the number of 3D queries. To select  $N_{3D}$  queries from the pool of  $V \times H \times W$  queries, we employ FPS (Farthest Point Sampling) (Qi et al., 2017) on the centers of the initial 3D Gaussians. Given the one-to-one correspondence between the 3D Gaussians and 3D queries, the 3D queries are subsequently downsampled based on the chosen 3D Gaussians.

Note that the number of camera queries can be much smaller than 3D queries due to the sparser nature of camera parameters requirements, we subsample a portion of the 2D reference points using FPS (Qi et al., 2017) based on the centroids of 3D Gaussians to obtain the reference points for camera parameters queries. For simplicity, we ignore the downsampling in the main paper. In the experiment, we use 256 queries for camera parameters in each view while 131,072 queries for 3D Gaussians.

### A.5 Details for deformable attention

After defining the reference points  $\mathbf{P}_i$ , image features,  $\mathbf{F}_i$ , and given the 3D queries  $\mathbf{Q}_{3D_i}$  for the  $i$ -th view, we do DFA on them to refine the queries. To sample the image features surrounding the reference points, trainable sampling offsets  $\Delta\mathbf{s} = \text{MLP}(\mathbf{q})$  are calculated, where MLP represents the multilayer perceptron layer comprising two linear layers and two activation functions. After that, the image features on the sampling points  $\mathbf{s} = \mathbf{P}_i + \Delta\mathbf{s}$  are sampled by grid sampling algorithm with bilinear interpolation, serving as the values  $\mathbf{v}$  for cross-attention. Then the attention score  $a_{3D_i} = \text{MLP}(\mathbf{Q}_{3D_i})$  is computed for the sampled image features at  $\mathbf{s}$ . Finally,  $\mathbf{Q}_{3D_i}$  is refined by dot product between the attention score and values. Consistent with (Zhang et al., 2023; Zhu et al., 2021), we derive attention scores directly from queries, omitting keys to simplify computations. The updating process of queries is shown in Fig. 7.

### A.6 More results

Table 8: Pose estimation performance in rotation error (e\_rot) and translation error (e\_trans) on RE10k, ACID. Methods with ‘\*’ meaning the model is trained on RE10k+DL3DV dataset, otherwise only on RE10K. ‘-A’ means with evaluation-time pose alignment.

Method	RE10k		ACID	
	e_rot ↓	e_trans ↓	e_rot ↓	e_trans ↓
NoPoSplat	4.258	2.879	11.269	3.296
NoPoSplat*	3.399	1.806	9.835	3.827
NoPoSplat-A	3.860	2.953	10.507	3.423
NoPoSplat-A*	2.948	1.912	10.448	3.488
Ours	3.704	2.295	11.087	3.192
Ours*	3.164	1.746	9.797	2.988
Ours-A	3.295	2.704	10.191	3.053
Ours-A*	2.746	1.838	9.815	3.234

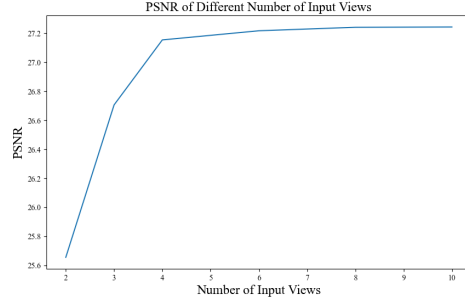
**Pose estimation performance** In addition to the pose estimation evaluated by AUC, we also provide the pose estimation performance in rotation error (e\_rot) and translation error (e\_trans) on RE10k, ACID in Table 8.

Table 9: Performance comparison on the evaluation set of pixelSplat for re10k dataset.

Method	PSNR ↑	SSIM ↑	LPIPS
pixelNeRF	20.43	0.589	0.55
GPNR	24.11	0.793	0.255
AttnRend	24.78	0.82	0.213
pixelSplat	26.09	0.863	0.136
MVSplat	26.39	0.869	0.128
NoPoSplat-A	26.786	0.878	0.124
Ours	25.837	0.852	0.129
Ours-A	27.214	0.891	0.118

**Performance on the evaluation set of pixelSplat** In order to conduct a fair comparison between our methods and the previous MVSplat benchmark, we evaluated our model using the indices provided in pixelSplat and MVSplat (Charatan et al., 2024; Chen, Yuedong and Xu, Haoifei and Zheng, Chuanxia and Zhuang, Bohan and Pollefeys, Marc and Geiger, Andreas and Cham, Tat-Jen and Cai, Jianfei, 2024). As depicted in Table 9, our model continues to outperform previous methodologies on the pixelSplat index.

**More number of input views** Our model is flexible and can receive an arbitrary number of input views, surpassing the limitations of only considering two views. We present the PSNR results for a larger number of input views, extending up to 10 views, in Fig. 8. Generally, more input views give better performance on scene reconstruction.



**Figure 8:** PSNR v.s. number of input views.

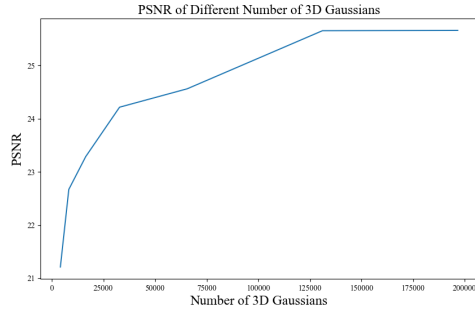


**Figure 9:** PSNR v.s. number of 3D Gaussians.

**Number of 3D Gaussians** We show the PSNR v.s. the number of 3D Gaussians in Fig. 9.

**More visualization** We provide more novel view synthesis results on RE10K and ACID with different groups of overlapping in this section Fig. 10, Fig. 11, Fig. 12, Fig. 13, Fig. 14, Fig. 15.



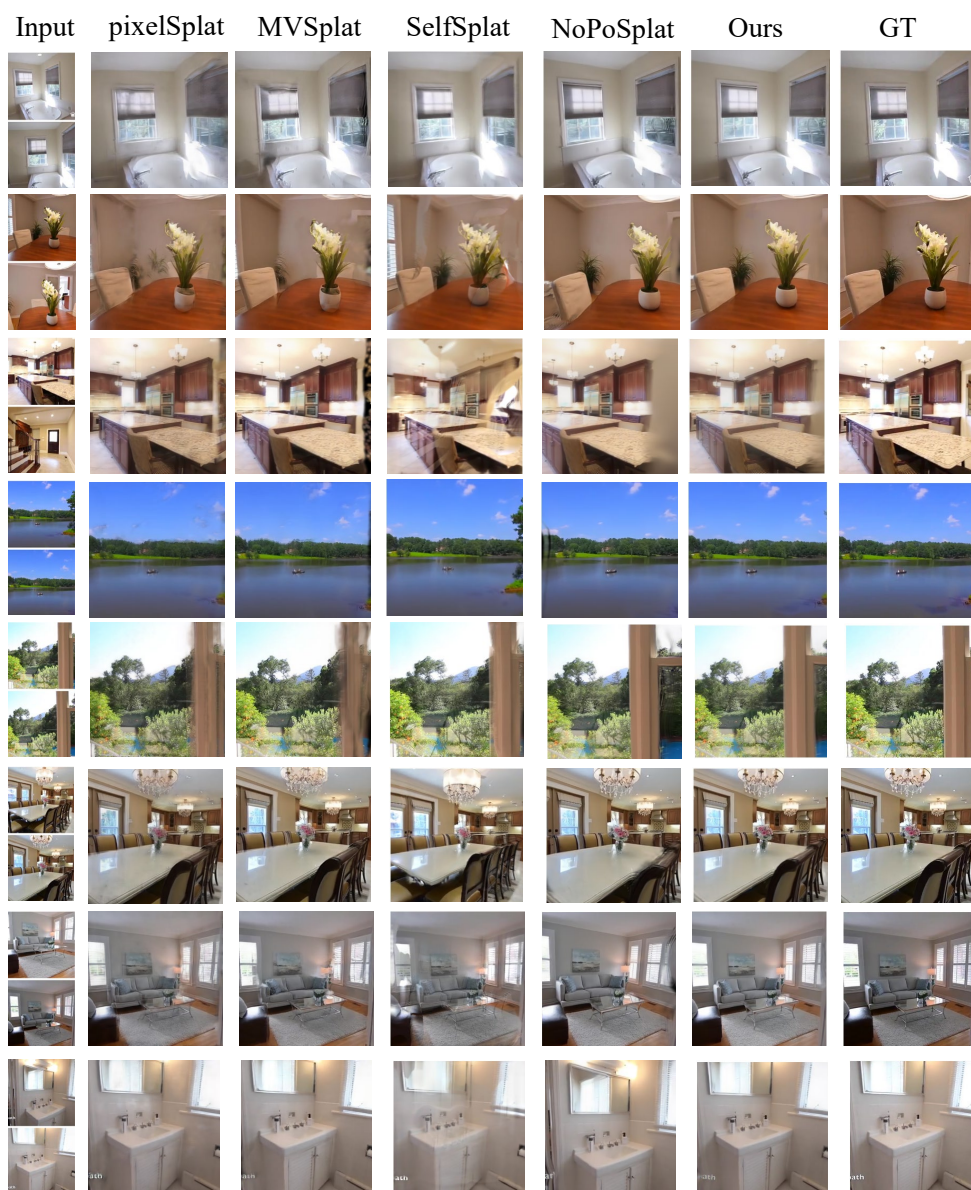


**Figure 10:** More comparisons of the RealEstate10K dataset with large overlap of input images.

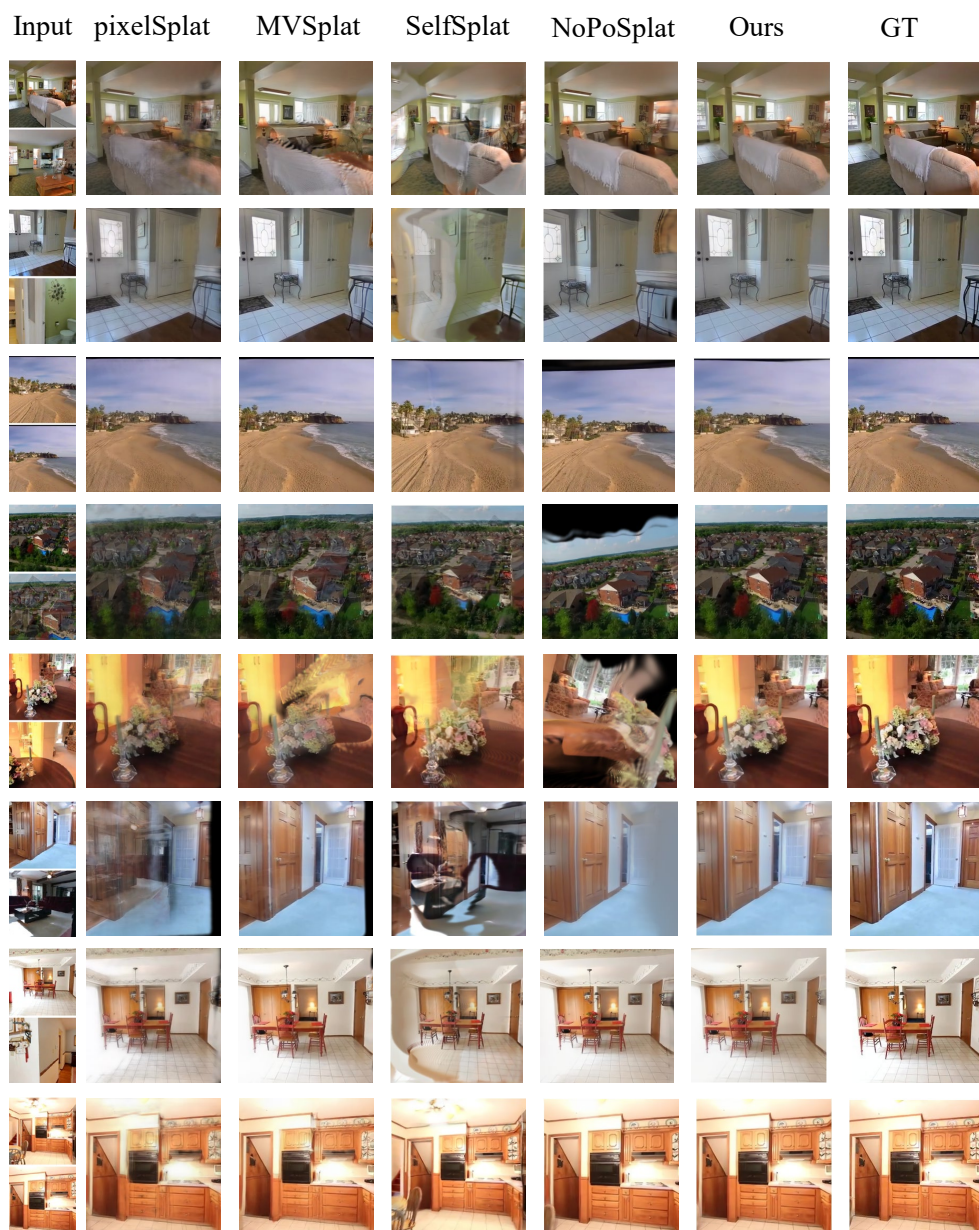


**Figure 11:** More comparisons of the RealEstate10K dataset with medium overlap of input images.



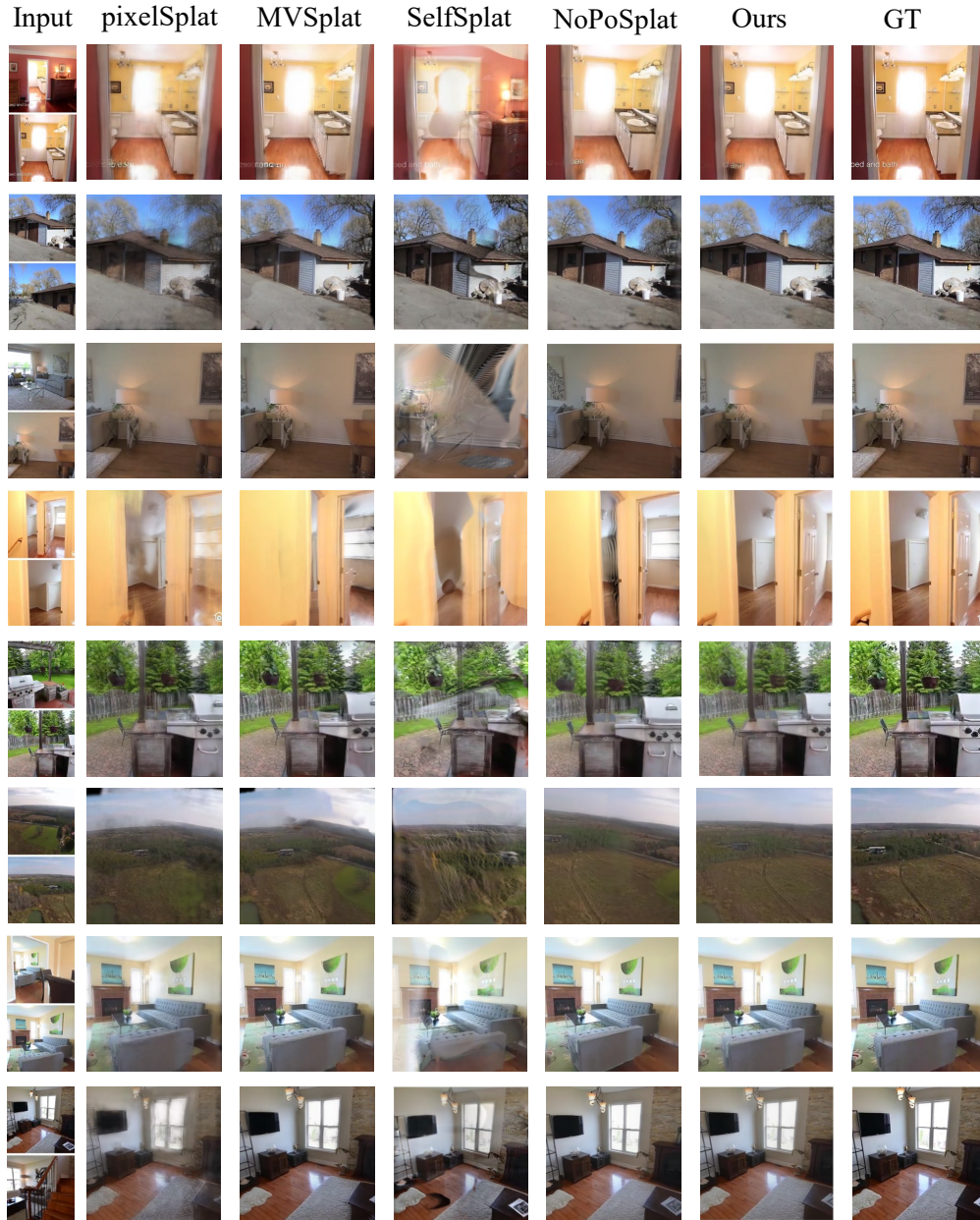


**Figure 12:** More comparisons of the RealEstate10K dataset with small overlap of input images.

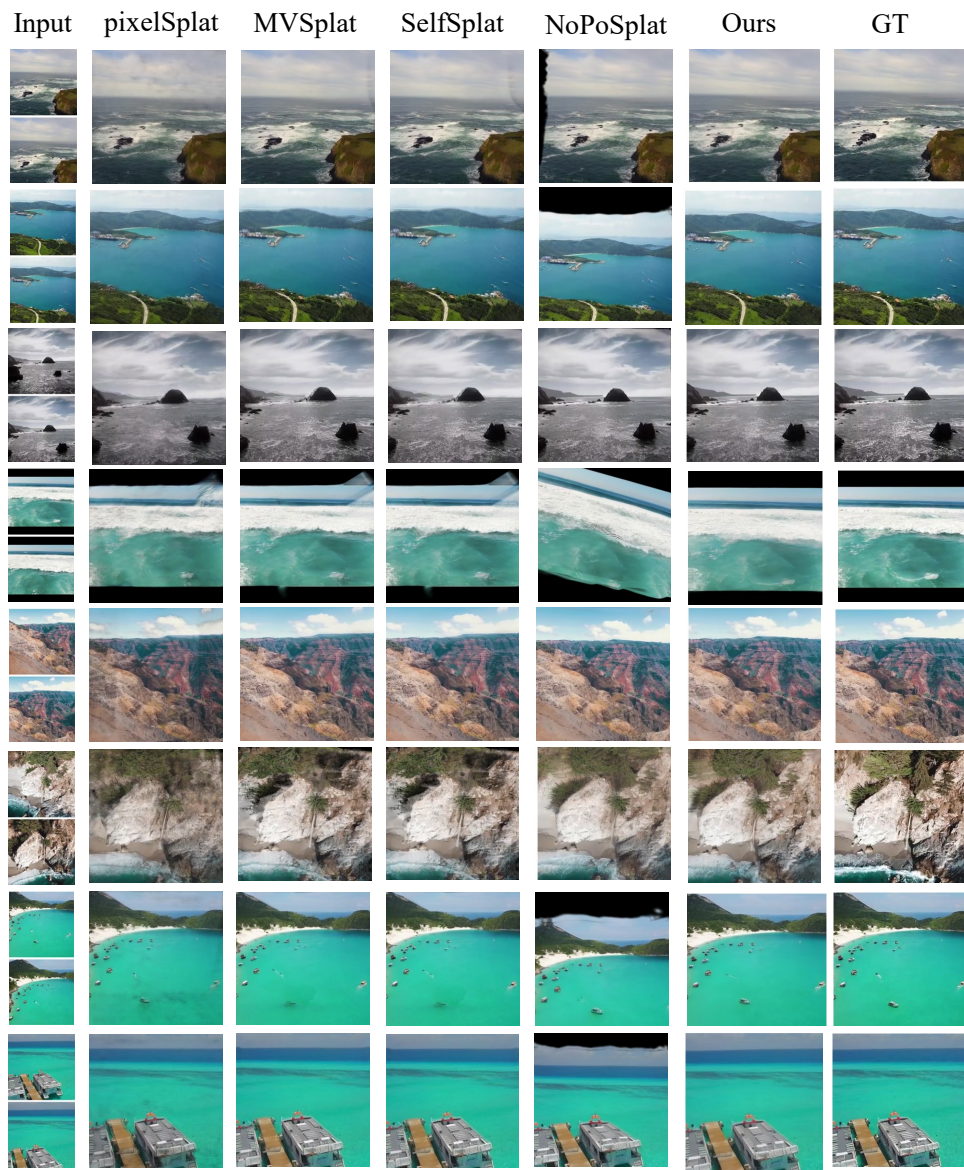


**Figure 13:** More comparisons of the ACID dataset with large overlap of input images.



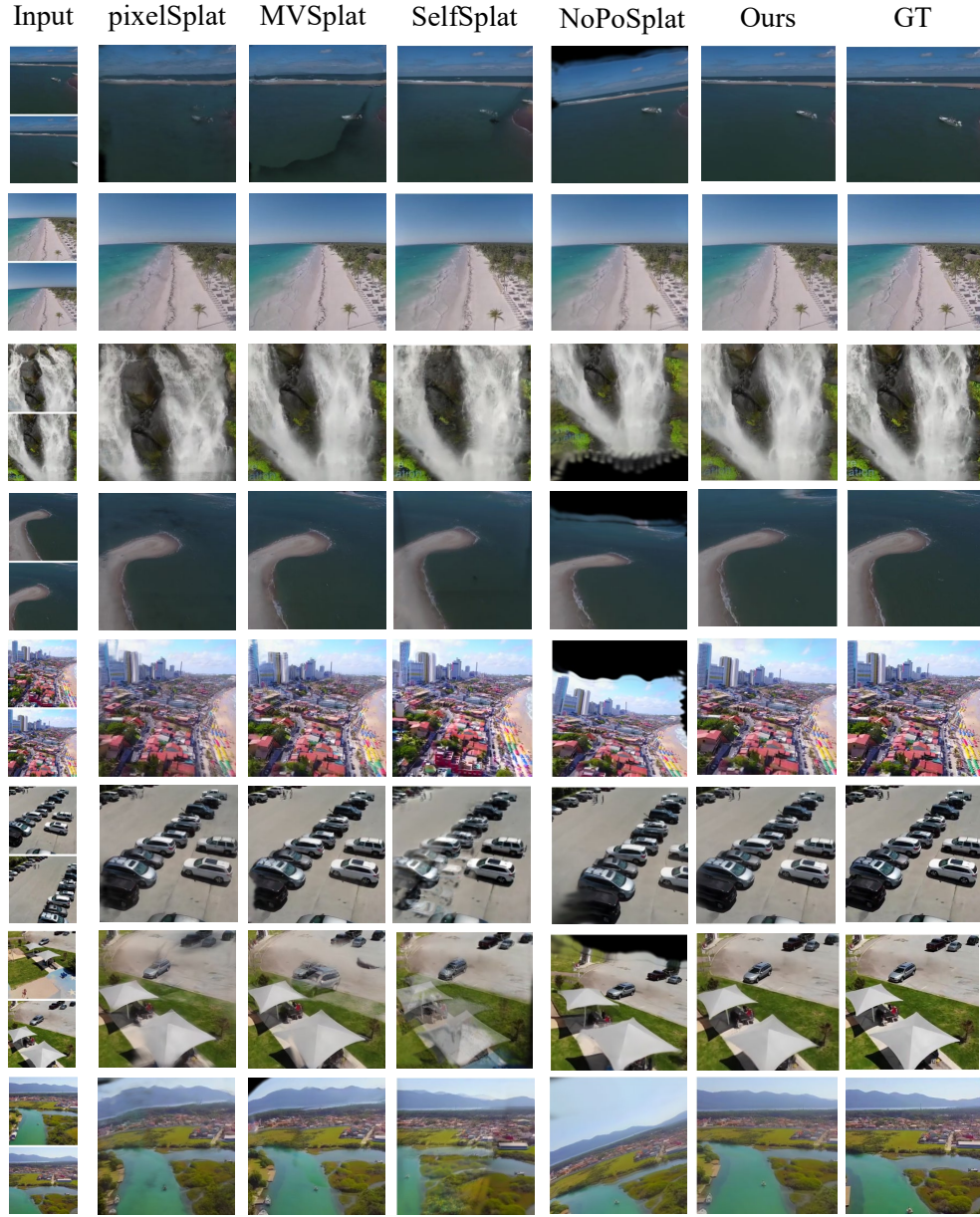


**Figure 14:** More comparisons of the ACID dataset with medium overlap of input images.

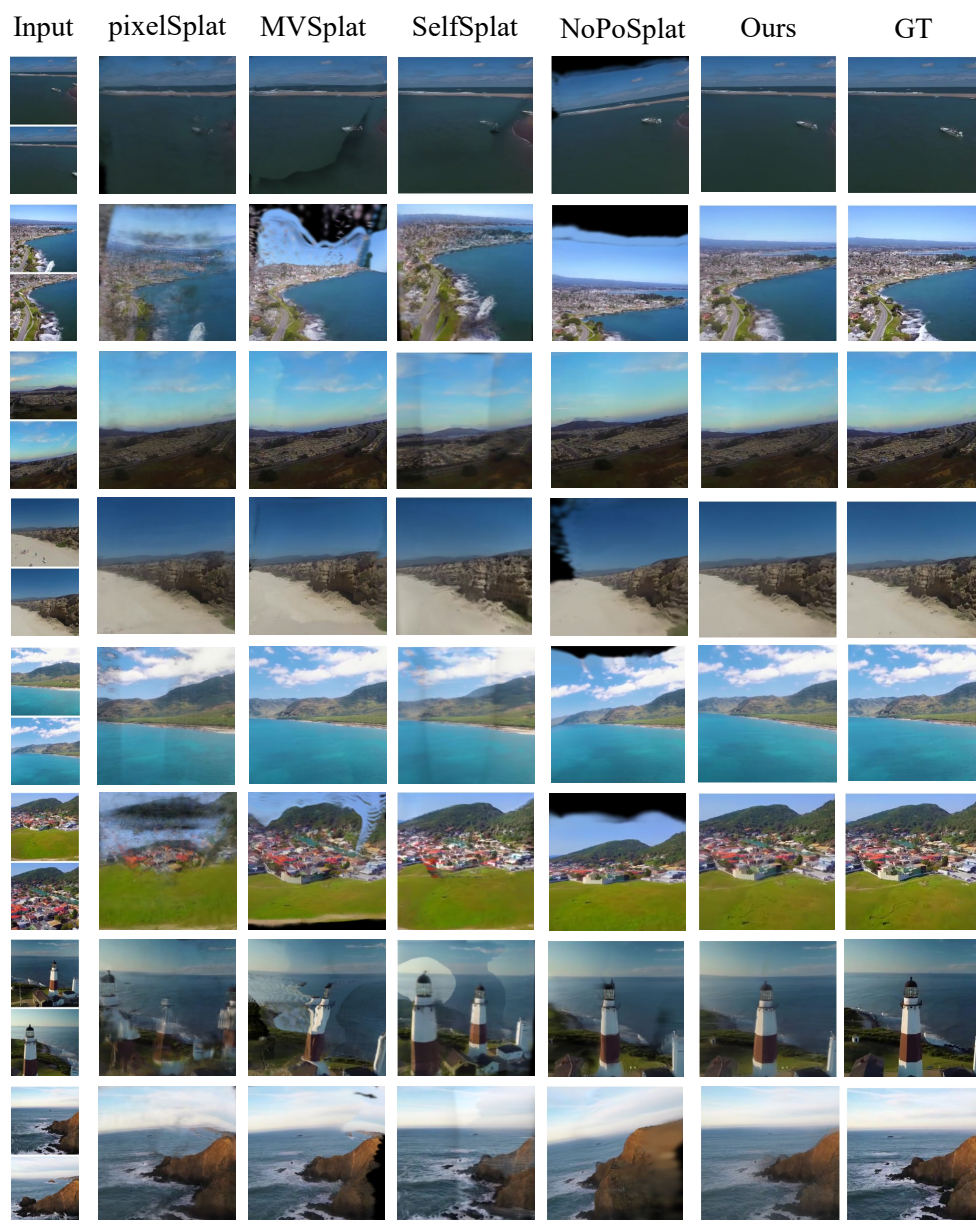


**Figure 15:** More comparisons of the RealEstate10K dataset with small overlap of input images.